Icarus 407 (2024) 115770

Contents lists available at ScienceDirect

Icarus

journal homepage: www.elsevier.com/locate/icarus

Insight from the Noachian-aged fractured crust to the volcanic evolution of Mars: A case study from the Thaumasia graben and Claritas Fossae

Bartosz Pieterek [a,*], Petr Brož [b], Ernst Hauber [c], Katrin Stephan [c]

[a] Geohazard Research Unit, Institute of Geology, Adam Mickiewicz University in Poznań, Poland
[b] Institute of Geophysics of the Czech Academy of Sciences, Prague, Czech Republic
[c] Institute of Planetary Research, DLR, Berlin, Germany

ARTICLE INFO

Keywords:
Volcanism
Thaumasia
CRISM
Effusive eruptions
Low-calcium pyroxene

ABSTRACT

Although most of the large volcanic landforms on Mars have been extensively studied, this is not the case for kilometer-sized landforms whose origin remains uncertain and which might provide important insights into the evolution of Martian volcanism. Previously, different populations of small-scale putative scoria cone volcanoes have been described in Tharsis, specifically in areas where the heavily fractured crust of the Noachian- and Hesperian-age escaped Amazonian resurfacing by younger lava flows. Therefore, we decided to explore a region of old fractured crust in Tharsis, Claritas Fossae, to search for signs of local-scale volcanic activity. Here, we present the results of a mapping campaign focused on the morphological and spectral properties of small-scale constructional mounds in the Noachian-age Claritas Fossae region that was affected by Hesperian- to early Amazonian-aged fracturing. By using data from Context Camera (CTX) and High Resolution Imaging Science Experiment (HiRISE), we mapped 39 mounds superimposed on the ancient crust and determined their morphological and morphometrical properties. The majority of the mounds are elongated (WNW- trending) with steep flanks and without associated flow units. The general appearance of studied edifices is consistent with a volcanic origin and their shapes suggest that they have been emplaced by effusion of viscous, volatile poor lavas incapable of significant flow. In addition, a spectral investigation utilizing the data from the Compact Reconnaissance Imaging Spectrometer for Mars (CRISM) reveal that some of the mounds showed evidence for high concentrations of low-calcium pyroxenes (LCP). Based on the relative stratigraphy, we demonstrate that volcanic activity is responsible for their formation and postdates the main N-S-trending fracturing of the Claritas Fossae, suggesting the formation of a volcanic field in the period spanning through the Late Hesperian and the Early Amazonian. However, morphological evidence such as well-preserved volcanic fissures and fresh-appearing slopes of some of the edifices might suggest even younger age. Among the mapped edifices, we found a well-preserved circular-shaped cone with a short-distance flow-like unit spreading from a caldera-like structure that challenges a scenario in which all the edifices are old. Such relatively young ages of volcanic activity combined with LCP-rich compositions might have critical implications for understanding the temporal evolution of magma compositions on Mars. Moreover, the observed shapes and spectral characteristics of the studied edifices appear to be quite different from other volcanic fields of similar geological settings observed so far on Mars. Therefore, we underline the importance of studying old and heavily fractured terrains that escaped later resurfacing by widespread younger lava flows, in order to search for evidence of small-scale volcanism and better understand local Martian magmatic systems.

1. Introduction

While large- to intermediate-scale Martian volcanic structures have been intensively studied in the past (e.g., Plescia and Saunders, 1982; Werner, 2009), kilometer-scale landforms have been partly overlooked due to the inadequate spatial resolution of the cameras orbiting Mars. Yet such small-scale landforms may record a complex volcanic history that has not been previously recognized by large-scale studies, providing a potentially significant contribution to the understanding of the evolutional history of Mars. With the increasing availability of high

* Corresponding author.
E-mail address: barpie@amu.edu.pl (B. Pieterek).

https://doi.org/10.1016/j.icarus.2023.115770
Received 14 March 2023; Received in revised form 25 July 2023; Accepted 28 August 2023
Available online 29 August 2023

resolution images of the Martian surface, the study of volcano-tectonic systems has been becoming more detailed (Keszthelyi et al., 2008; Robbins et al., 2011). Currently, the general knowledge about the major volcano-tectonic units on Mars, especially for the Tharsis Volcanic Province, seems to be well-constrained (Bouley et al., 2018; Mouginis-Mark et al., 2021) as they constitute the main focus of interest through decades. Considering the magmatic system(s) of the Tharsis rise, it comprises giant volcanoes (Wilson et al., 2001; Plescia, 2004) accompanied by hundreds of smaller distributed volcanoes in the central part (Hauber et al., 2009; Richardson et al., 2021; Pieterek et al., 2022a) and two volcanic centers, Syria Planum (Baptista et al., 2008; Richardson et al., 2013) to the south and Tempe Terra (Baratoux et al., 2009; Hauber et al., 2009) to the northeast. Recent results suggest that volcanic activity in Tharsis has most probably started at > 4.0 Ga (Breuer and Moore, 2015), and continued with episodes of enhanced magma supply (Wilson et al., 2001) until the Late Amazonian (Hartmann et al., 1999; Neukum et al., 2004; Hauber et al., 2011; Lagain et al., 2021; Krishnan and Kumar, 2022; Pieterek et al., 2022a). Besides the major volcanoes of Tharsis, which represent the first episodes of growth in the Noachian period ($>$ 3.9 Ga; Platz et al., 2011; Robbins et al., 2011), Noachian volcanoes have been also observed in the southern part of Tharsis including the Thaumasia region (Dohm and Tanaka, 1999; Grott et al., 2005, 2007).

Both the giant as well as kilometer-scale volcanoes in Tharsis that have been studied so far were mostly classified as low-shield volcanoes indicating effusive eruptions (Bleacher et al., 2007; Hauber et al., 2009; Zimbelman et al., 2015; Richardson et al., 2021) of low-viscosity basaltic magmas (Mangold et al., 2010; Viviano-Beck et al., 2017). On the other hand, unambiguous evidence for explosive volcanism on Mars is rare and mainly restricted to ancient terrains ($>$ 3.5 Ga; e.g., Apollinaris Mons; Wilson and Head, 2007; Kerber et al., 2011; the Circum-Hellas province; Crown et al., 2021; see Brož et al., 2021 for a recent review). However, in the last decade, high-resolution images allow recognition of several sites where explosive volcanism might be present even in Tharsis and its closest surroundings. Namely, scoria cones have been reported on the flanks of large low-shield volcanoes (Edgett, 1990; Bleacher et al., 2007; Hauber et al., 2009), in Ulysses Fossae (Brož and Hauber, 2012), Coprates Chasma (Brož et al., 2017), Hydraotes Chaos (Meresse et al., 2008) and Noctis Fossae (Pieterek et al., 2022b). While possible volcanic edifices in Coprates Chasma and Hydraotes Chaos are superposed on young sedimentary infill, those in Ulysses and Noctis Fossae are superposed on an old, heavily fractured crust that escaped resurfacing by younger basaltic lava flows.

The Ulysses Colles mound field comprises well-preserved conical edifices accompanied by short flows that are structurally controlled by extensive N- to NNW-trending normal faults. They have been interpreted as Martian scoria cones associated with lava flows (Brož and Hauber, 2012). These putative volcanic edifices are superimposed on an older crust that is dated to the early Hesperian (Anderson et al., 2001), whereas their formation was estimated to occur between 1.5 and 0.4 Ga (Brož and Hauber, 2012). Similar to Ulysses Colles, the putative scoria cones from Noctis Fossae are also superimposed on an older crust, dated to Late Hesperian (Tanaka et al., 2014), and mostly dominated by NNE-trending faults. These tectonic structures were likely formed in the Noachian due to a single transtension event that was probably later slightly modified to NWW direction by a lateral component of displacement (Bistacchi et al., 2004). The estimated age of the Noctis Fossae cones' formation range between 2.0 Ga and 0.05 Ga (Pieterek et al., 2022b). Therefore, these studies indicate that volcanic edifices might have been preserved on old fractured terrains.

Additionally, it was also proposed by Robbins et al. (2011) that volcanic activity on Mars might change from an explosive to an effusive style of eruptions at the transition between the Noachian and the Hesperian, at approximately 3.5 Ga. Another key transition in the magmatic history of Mars should occur in a similar time frame with the change in the mineralogical and chemical compositions of magmatic products transitioning from low- (LCP) to high-calcium (HCP) pyroxenes contents (Mustard et al., 2005; Poulet et al., 2009). Therefore old, heavily fractured elevated regions that escaped younger volcanic activity might constitute a window where it might be possible to investigate the style of volcanism that might have been common before the latest stage of plain-style volcanism covered most of Tharsis (e.g., Hauber et al., 2009, 2011; Richardson et al., 2021; Brož and Hauber, 2011).

To further test this hypothesis, we performed a mapping campaign focusing on the search for small-scale volcanic edifices in the southern region of Tharsis, in the Thaumasia region, which comprises topographic belts affected by Noachian- to early Hesperian-aged faulting (Dohm and Tanaka, 1999; Smith et al., 2009; Vaz et al., 2014). We investigated and mapped an unnamed cluster of positive topographic landforms (mounds) that are located in the Claritas Fossae region, one of the mountainous highlands surrounding the Thaumasia plateau (Fig. 1). Our goal was to determine the geological origin of the studied mounds and, should they indeed be of volcanic origin, to provide insight into their eruption style and the composition of their parental magmas. Moreover, as the spatial distribution of volcanic edifices and their alignments can reveal tectonic stress orientations and the geometry of the underlying feeder dikes (Corazzato and Tibaldi, 2006; Acocella and Neri, 2009; Paulsen and Wilson, 2010; Pieterek et al., 2022a), our study might also improve the knowledge of magma emplacement mechanisms and the evolution of tectonic processes within Claritas Fossae.

2. Geological settings

The study area is situated within the Thaumasia region in the southeastern part of the Tharsis rise, the largest volcano-tectonic province on Mars (Fig. 1a). The central part of the Thaumasia region consists of three plateaus (Solis Planum, Sinai Planum, Thaumasia Planum). They are surrounded by a Noachian-Hesperian highland belt (Anderson et al., 2001) and consist mostly of Hesperian lava plains (from 3.66 Ga to 3.14 Ga; Ruj and Kawai, 2021). The Thaumasia mountainous highland belt comprises the Coprates Rise (formed from 4.1 to 3.0 Ga; Schultz and Tanaka, 1994; Dohm and Tanaka, 1999), Coracis Fossae (from 3.9 to 3.5 Ga; Grott et al., 2005), and Claritas Fossae (from 4.2 to 3.4 Ga; Vaz et al., 2014) to the southeast. To the north, the Thaumasia plateau is surrounded by the volcanically long-lived Syria Planum dome (from $>$4.0 Ga up to 0.4 Ga; Hauber et al., 2011; Xiao et al., 2012) (Fig. 1a) and the Valles Marineris. The Claritas and Coracis Fossae that characterize the heavily cratered highland belts together with the western part of Solis Planum were formed by several episodes of extensional faulting (Hauber and Kronberg, 2005) and form a complex system of faults segments, grabens, and halfgrabens bounded by normal faults (Vaz et al., 2014; Balbi et al., 2022). The majority of these faults are characterized by lengths of $<$300 km and orientations ranging from N180 to N090 (Bouley et al., 2018) with a mean dip of $\sim 41^\circ \pm 8^\circ$ (Vaz et al., 2014). Dohm and Tanaka (1999) demonstrated that these faults were likely formed and/or reactivated over a long period of time. They have been developing from Early to Middle Noachian, the rate for formation then declined during Late Noachian and Early Hesperian, and substantially diminished during Late Hesperian/Amazonian. Moreover, Anderson et al. (2001) demonstrated that the tectonic activity in this region peaked in Noachian. Concerning the absolute age of the N-S-trending faulting, Smith et al. (2009) determined the age ranging between 3.3 and 2.5 Ga using fault-buffered crater counts. These estimations were further supported by surface age determination provided by Vaz et al. (2014), who conclude that the faulting in the Claritas Fossae region had occurred between 3.37 $\pm$ 0.08 and 2.55 $\pm$ 0.23 Ga. The most recent study conducted by Balbi et al. (2022) demonstrated that the Claritas Fossae region has been affected by a long-lasting tectonic deformation history comprised of multiple reactivations of crustal weakness zones, however, without providing any age constraints about the tectonic evolution.

During the last stage of the main phase of the Thaumasia tectonics,

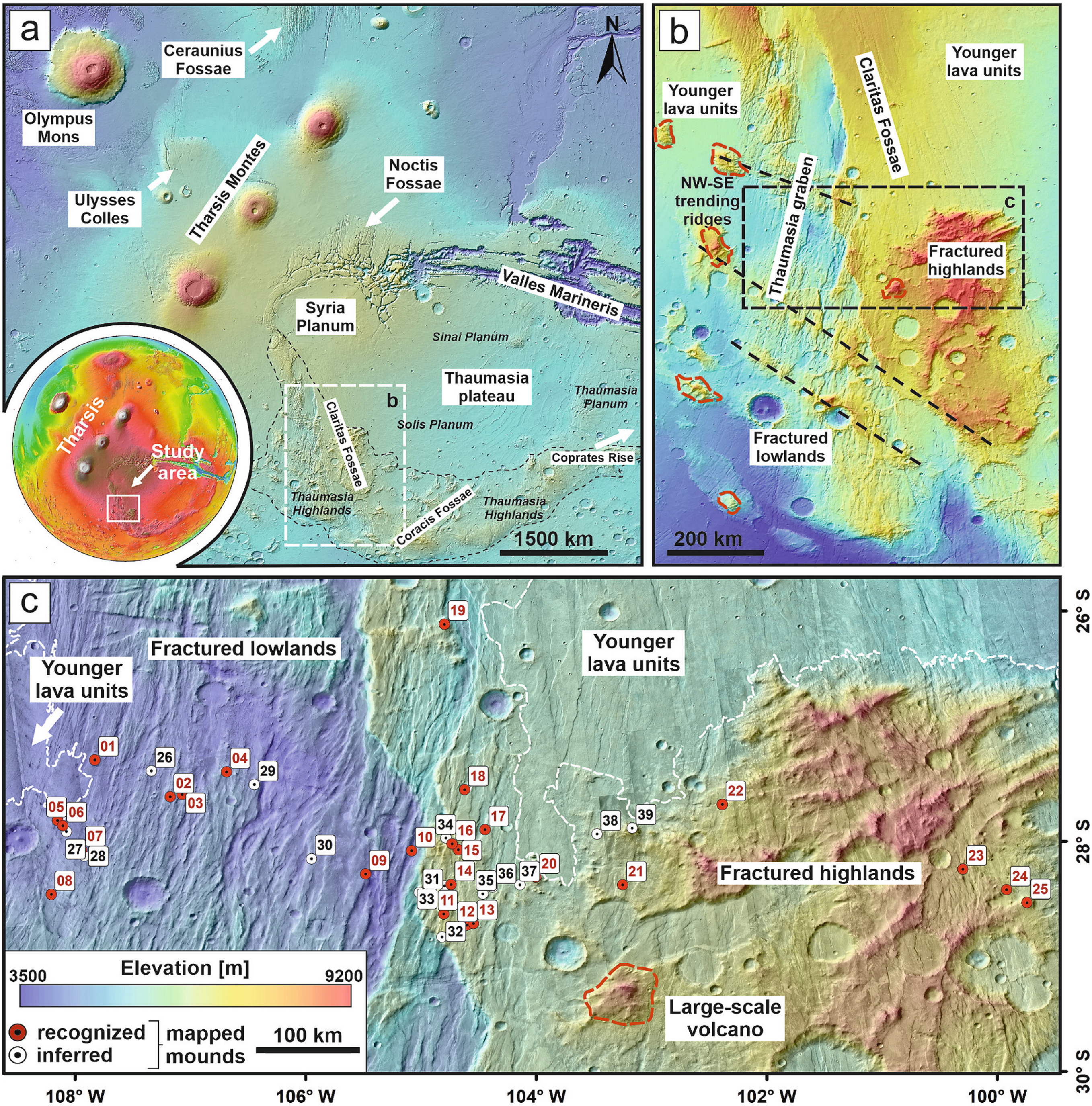

Fig. 1. (a) An overview topographic map of the Tharsis Volcanic Province including Claritas Fossae and Thaumasia region. This map indicates the locations of the volcanic fields Ulysses Colles (Brož and Hauber, 2012) and Noctis Fossae (Pieterek et al., 2022b). The left inset shows the location of Tharsis with the rectangle indicating the location of the study area. **(b)** Topographic map of the large Thaumasia graben and the Claritas Fossae region with NW-SE-trending ridges distinguished by Hauber and Kronberg (2005) that are perpendicularly oriented to the main faults and structures of the region. The map is a combination of a blend of digital elevation model (200 m/px; Fergason et al., 2018) data derived from the Mars Orbiter Laser Altimeter (MOLA) and High-Resolution Stereo Camera (HRSC) and MOLA shaded relief basemap adapted from Tanaka et al. (2014). The red dashed lines mark the location of the topographic rises interpreted as volcanoes by Dohm and Tanaka (1999). **(c)** A topographic map of the study area showing the spatial distribution of mapped mounds classified into two classes. The white dashed lines mark the extent of younger lava flows originated from the north, whereas the red dashed line marks the location of the large-scale volcano described by Dohm and Tanaka (1999). The basemap constitutes the modification (higher transparency) of the map from panel (b) overlaid by the image mosaic of the Context Camera system (acquired from GeoScience PDS Node). The numbers of the mapped edifices correspond to the locations of features depicted in the next figures. (For interpretation of the references to colour in this figure legend, the reader is referred to the web version of this article.)

probably in Late Hesperian or Early Amazonian (Tanaka and Davis, 1988; Hauber and Kronberg, 2005), the Thaumasia graben, a 100-km wide and 1000-km long N020W-trending structure, was superimposed on the Noachian-age graben system of Claritas Fossae (Hauber and Kronberg, 2005) (Fig. 1b). The eastern wall (bounding fault) of the Thaumasia graben divides the Claritas Fossae region into the western heavily fractured lowlands (ranging from ~3500 m up to ~5200 m above the Mars datum surface) and eastern moderately fractured highlands (from ~5500 up to ~9200 m above the datum) (Fig. 1b). This fault is interpreted as a listric normal fault that reaches the base of the crust at a depth of ~80 km (Balbi et al., 2022). In addition, Hauber and Kronberg (2005) highlighted that south of 24°S, the Thaumasia graben and Claritas Fossae are crossed by WNW-ESE-trending topographic highs of rugged Noachian terrain (Fig. 1b). These topographic highs likely represent ancient highland ridges (predating the tectonic activity forming N-S-trending grabens) that are buried in their NW parts under younger lava plains (Fig. 1b). These younger lava plains extend on both sides of Claritas Fossae, showing their origin from the north with the source regions of Tharsis and Syria Planum to the west and east, respectively (Fig. 1b-c). In addition, Vaz et al. (2014) showed low scarp degradation rates (4.0×10^{-3} m^2/kyr) for Claritas Fossae over the last 3 billion years indicating a negligible effect of erosion throughout the geological history of the studied area. However, it should be considered that the faulting in the studied region occurred in several phases spacing from the Noachian to Amazonian ages (Dohm and Tanaka, 1999), therefore the states of scarps preservation should vary. This is also expressed in the westernmost part of Thaumasia graben as this region is affected by younger lava flows. The moderate amount of faults that are present on these flows indicates that these lava flows are likely younger than the main N-S faulting but older than the younger generation of

Table 1
Selected information regarding images from the High-Resolution Stereo Camera (HRSC), Context Camera (CTX), High Resolution Imaging Science Experiment (HiRISE), and Compact Reconnaissance Imaging Spectrometer for Mars (CRISM) used for this study.

Image ID	Imagery system	Center Latitude	Center Longitude	Ground pixel resolution	Acquisition time	Subsolar azimuth	Incidence angle
B11_014063_1523	CTX	27.78°S	259.70°E	5.07 m/pixel	27 July 2009	193.64°	34.36°
B20_017439_1503	CTX	29.84°S	253.20°E	5.10 m/pixel	16 April 2010	230.26°	72.58°
B21_017650_1537	CTX	26.38°S	252.19°E	5.16 m/pixel	02 May 2010	229.48°	71.01°
B21_017729_1510	CTX	29.07°S	254.92°E	5.11 m/pixel	08 May 2010	230.05°	72.64°
D08_030177_1509	CTX	29.14°S	253.55°E	5.07 m/pixel	02 January 2013	184.39°	46.70°
D09_030599_1527	CTX	27.42°S	251.76°E	5.10 m/pixel	04 February 2013	179.63°	41.25°
D15_033091_1519	CTX	28.18°S	254.83°E	5.09 m/pixel	17 August 2013	222.08°	48.2°
D17_033737_1522	CTX	27.86°S	257.65°E	5.07 m/pixel	07 October 2013	226.41°	57.95°
F08_038933_1514	CTX	28.63°S	254.44°E	5.03 m/pixel	16 November 2014	183.48°	49.79°
G05_020063_1536	CTX	26.42°S	253.75°E	5.11 m/pixel	06 November 2010	204.93°	60.80°
G17_024955_1524	CTX	27.68°S	255.07°E	5.07 m/pixel	23 November 2011	227.35°	57.56°
G18_025100_1524	CTX	27.70°S	256.39°E	5.07 m/pixel	04 December 2011	228.04°	59.56°
G20_026221_1550	CTX	25.03°S	252.38°E	5.12 m/pixel	29 February 2012	230.15°	68.02°
J07_047570_1518	CTX	28.25°S	255.71°E	5.07 m/pixel	19 September 2016	188.09°	47.53°
K13_058449_1496	CTX	30.41°S	257.10°E	5.10 m/pixel	14 January 2019	208.55°	32.89°
P13_005954_1529	CTX	27.17°S	259.90°E	5.11 m/pixel	03 November 2007	210.6°	38.16°
P17_007800_1525	CTX	27.58°S	255.96°E	5.12 m/pixel	26 March 2008	227.8°	64.86°
P18_007945_1532	CTX	26.89°S	255.27°E	5.46 m/pixel	06 April 2008	228.41°	65.11°
ESP_012362_1515	HiRISE	28.344°S	260.079°E	50 cm/pixel	16 March 2009	4.1°	51°
ESP_012771_1520	HiRISE	27.629°S	252.848°E	50 cm/pixel	17 April 2009	359.5°	45°
ESP_076675_1525	HiRISE	27.279°S	252.177°E	50 cm/pixel	04 December 2022	349.0°	43°
ESP_076656_1510	HiRISE	28.521°S	260.223°E	50 cm/pixel	25 November 2022	344.2°	42°
ESP_076767_1510	HiRISE	28.514°S	260.311°E	50 cm/pixel	12 December 2022	352.7°	44°
ESP_076833_1510	HiRISE	28.523°S	260.313°E	49 cm/pixel	17 December 2022	353.3°	46°
ESP_076899_1510	HiRISE	28.526°S	260.226°E	51 cm/pixel	22 December 2022	357.9°	47°
ESP_077031_1514	HiRISE	28.294°S	254.558°E	53 cm/pixel	01 January 2023	3.1°	47°
FRT0000A91D	CRISM	28.22°S	254.64°E	18 m/ pixel	22 April 2008	–	68.6°
FRT0001C5B6	CRISM	27.95°S	256.83°E	18 m/ pixel	10 December 2010	–	56.5°
HRS000119AF	CRISM	28.35°S	260.09°E	36 m/ pixel	16 March 2009	–	51.4°
HRS00012172	CRISM	27.64°S	252.86°E	36 m/ pixel	17 April 2009	–	45.4°
Digital elevation model							
H0530_0000_DA4	HRSC	25.43°S 41.50°S	256.27°E 263.48°E	150 m/pixel	12 June 2008	–	–
Pair 1							
P13_005954_1529	CTX stereo	27.17°S	259.90°E	5.11 m/pixel	03 November 2007	210.6°	38.16°
K15_059095_1529	CTX stereo	27.20°S	259.95°E	5.22 m/pixel	06 March 2019	217.33°	39.85°
Pair 2							
P18_007945_1532	CTX stereo	26.89°S	255.27°E	5.46 m/pixel	06 April 2008	228.41°	65.11°
N10_066414_1533	CTX stereo	26.81°S	255.14°E	5.08 m/pixel	26 September 2020	180.14°	39.79°
Pair 3							
D09_030599_1527	CTX stereo	27.42°S	251.76°E	5.10 m/pixel	04 February 2013	179.63°	41.25°
K17_059926_1494	CTX stereo	30.64°S	252.01°E	5.19 m/pixel	09 May 2019	228.26°	54.24°
Pair 4							
J20_052765_1519	CTX stereo	28.21°S	260.25°E	5.09 m/pixel	28 October 2017	231.86°	69.91°
K15_059095_1529	CTX stereo	27.20°S	259.95°E	5.22 m/pixel	06 March 2019	217.33°	39.85°
Pair 5							
K09_056840_1490	CTX stereo	31.03°S	257.07°E	5.07 m/pixel	11 September 2018	185.33°	42.11°
K13_058449_1496	CTX stereo	30.41°S	257.10°E	5.10 m/pixel	14 January 2019	208.55°	32.89°

HiRISE resolutions are given for map-projected images.

superimposed faults (Fig. 1c). Therefore, the Noachian-aged crust of Claritas Fossae, exposed on the Martian surface, represents a window to ancient terrains that escaped the later resurfacing caused by widespread younger lava flows (Tanaka and Davis, 1988; Brož and Hauber, 2011).

Besides the ubiquitous traces of tectonic activity in the Thaumasia region, there is evidence that volcanism was particularly active in comparison with other Martian cratered highlands (Dohm and Tanaka, 1999). Based on the geologic map of the Thaumasia region by Dohm and Tanaka (1999), the highland belt of the Thaumasia region seems to be associated with fourteen large topographic rises (Fig. 1b-c), which are interpreted as possible volcanoes (Dohm and Tanaka, 1999; Grott et al., 2007). Based on the detailed mapping, Grott et al. (2005) set a lower age limit of their formation of 3.9 Ga as these putative volcanoes are cut by rift-related faults and therefore predate the rifting. The age of the eastern Coracis Fossae faulting was estimated based on crater counts of the rift-related fault segments and intra-rift lava plains that revealed ages ranging from 3.9 to 3.5 Ga, respectively. Considering the spatial distribution of these volcanoes, they are NW-SE aligned (for more details see Fig. 8 in Dohm and Tanaka (1999)) and show complex morphologies that might indicate interbedded lavas and pyroclastic deposits originated from explosive eruptions (Dohm and Tanaka, 1999).

Based on the dust distribution map, the Claritas Fossae region is characterized by a moderate to low degree of dust mantling (Ruff and Christensen, 2002). The inspection of High Resolution Imaging Science Experiment (HiRISE) images shows the presence of aeolian landforms such as dunes and ripples, especially on the grabens' floors (Vaz et al., 2014). In addition, the presence of morphological evidence of glacial landforms within large impact craters at mid-latitudes (from 39°S to 42°S) in the Thaumasia highlands standing mostly higher than 5000 m in altitude was reported by Rossi et al. (2011).

3. Methods

To search for and map the mounds we used Context Camera images (CTX) onboard the Mars Reconnaissance Orbiter (MRO; Malin et al., 2007). CTX images have a spatial scale of ~5 m/px (Table 1), which is sufficient to identify kilometer-sized positive topographic landforms (Figs. 2 and 3) as well as associated flow-like features. To provide more detailed observations, we also used eight HiRISE images (also onboard MRO) for selected areas with a ground sampling distance of 50 cm/px (Table 1) (McEwen et al., 2007). The elevation data for the entire study area were acquired from a blended digital elevation model (200 m/px; Fergason et al., 2018) derived from the Mars Orbiter Laser Altimeter (MOLA; Smith et al., 2001) and the High-Resolution Stereo Camera (HRSC; Gwinner et al., 2016). To conduct a detailed topographic analysis of several individual mounds, we used digital elevation models (DEMs) derived from CTX stereo pair images. To achieve this, we used a data processing information system called MarsSI (Mars System of Information) aimed to process Martian orbital data (Quantin-Nataf et al., 2018). The CTX-based DEMs show a cell size of ~12 m/px and a vertical accuracy of ~4 m allowing us to conduct precise topographic measurements. Among the entire set of mapped mounds (39), the high-resolution CTX-based DEMs are available for 10 of them. Based on the Grosse et al. (2012) methodology, we determined the basic morphological parameters of the mapped mounds including basal length (L_{CO}; measured along the longest axis), basal width (W_{CO}; measured perpendicularly to the elongation); area of the mound basement (A_{CO}), the basal mound elevation (H_{CO}), the elevation of the summit (H_{CR}; measured at the highest point of the mound), the relative height of the mound (H; calculated as the difference between H_{CR} and H_{CO}), and mean and maximum flank slope angles of the mounds (Table 2). The spatial extent of the mapped mounds (basal area) was determined using the CTX images supported by elevation data and defined as the maximum extent of the deposits associated with the mapped landforms (Fig. 4). The elevation of the mound basement was established as the lowest elevation defined by the perimeter of the mapped mound. For small mounds <1 km diameter (at least in one axis) that were not covered by the high-resolution CTX-based DEM, we did not measure the topographic parameters due to the limited resolution of the MOLA-HRSC blended DEM (Table 2). Although we determined the topographic data for >1 km large mounds using the MOLA-HRSC-based DEM (Table 1), these results should be considered with caution due to the insufficient resolution for investigating small-scale landforms (Brož et al., 2015). The high-resolution topographic data derived from CTX stereo pairs were used to perform the slope analysis (Fig. 4) and calculate the volume of the mounds (Fig. 4). To compare morphological parameters to other Martian volcanic edifices (Fig. 4), we only used morphological data determined based on high-resolution CTX-derived DEMs (Table 2). In addition, using CTX images, we measured the orientations of the mounds` elongation, which was determined along the central fissure or the longest axis of the studied mound. The image and data analysis were conducted using ArcGIS software version ArcMap 10.5. The slope analysis and volume calculations were conducted by applying the Slope Analysis and Volume tools in the 3D Analyst ArcToolbox. In the volumetric calculations, the basal mound elevation was set as the reference plane elevation. Terrestrial data for comparative analyses were obtained from Google Earth™ (Inc, 2021) and are based on the Landsat/Copernicus, Maxar Technologies, and CNES/Airbus satellite imagery.

Among the entire mapped field, the mounds show variable sizes (from ~1 km along the longest axis up to several kilometers; Table 2) and diverse morphological characteristics. In order to differentiate the mapped mounds, we classified them into one of two groups, namely "recognized" and "inferred" (Fig. 1; Table 2). The "recognized" class is represented by the mounds for which we were able to conduct detailed analyses or reveal diagnostic morphological features allowing us to determine their putative origin. The "inferred" class was determined mostly for small-scale positive topographic landforms (typically <3 km in diameter) which are emplaced in the vicinity of the "recognized" mounds and for whose we were unable to conduct detailed analysis or reveal diagnostic morphological features allowing us to determine their putative origin. In the text and figures, we have used the CF abbreviation which stands for Claritas Fossae mounds.

To investigate the mineralogical composition of the mapped mounds, we used hyperspectral data (Table 1) that were acquired by the Compact Reconnaissance Imaging Spectrometer for Mars (CRISM; spatial scale and spectral resolution of 15–19 m/px and 362–3920 nm at 6.55 nm/channel, respectively) onboard the MRO (Murchie et al., 2007). For spectral analysis, we mainly focused on the 1.0–2.6 μm range, which includes the key spectral features of both mafic and hydrated minerals (Viviano-Beck et al., 2014). We avoid the detector boundary at 1 μm and the lower-signal region beyond the deep atmospheric CO_2 band at ~2.7 μm. However, we analyzed also the 0.4–1.0 μm range for the HRS00012172 image (fully covering the investigated mounds) to provide more spectral data for our mineralogical interpretation. The raw CRISM data (product files of IR hyperspectral image) were downloaded from the NASA Planetary Data System (PDS). The CRISM I/F data were analyzed using the CRISM Analysis Toolkit (CAT) developed for the Environment for Visualizing Images/Integrated Development Language (ENVI/IDL) software system (Morgan et al., 2017). Using the CAT software, CRISM data were imported from the PDS version into ENVI and standard photometric and atmospheric corrections were applied (McGuire et al., 2009; Murchie et al., 2009). In addition, we included the volcano-scan correction algorithm for atmospheric CO_2 migration, which allows for the improved detection of minerals with intrinsic absorption bands at wavelengths between 1.9 and 2.1 μm (McGuire et al., 2009). To better identify the region of interest for further detailed spectral investigation, we applied the Spectral Analysis Utilities used to derive the CRISM spectral summary products (Pelkey et al., 2007; Viviano-Beck et al., 2014) that were projected on the CRISM band parameter maps. Based on IR-derived products (D2300, LCPINDEX2, and HCPINDEX2), we selected areas of interest for spectral analysis (the numerators were mostly comprised of several pixels) characterized by

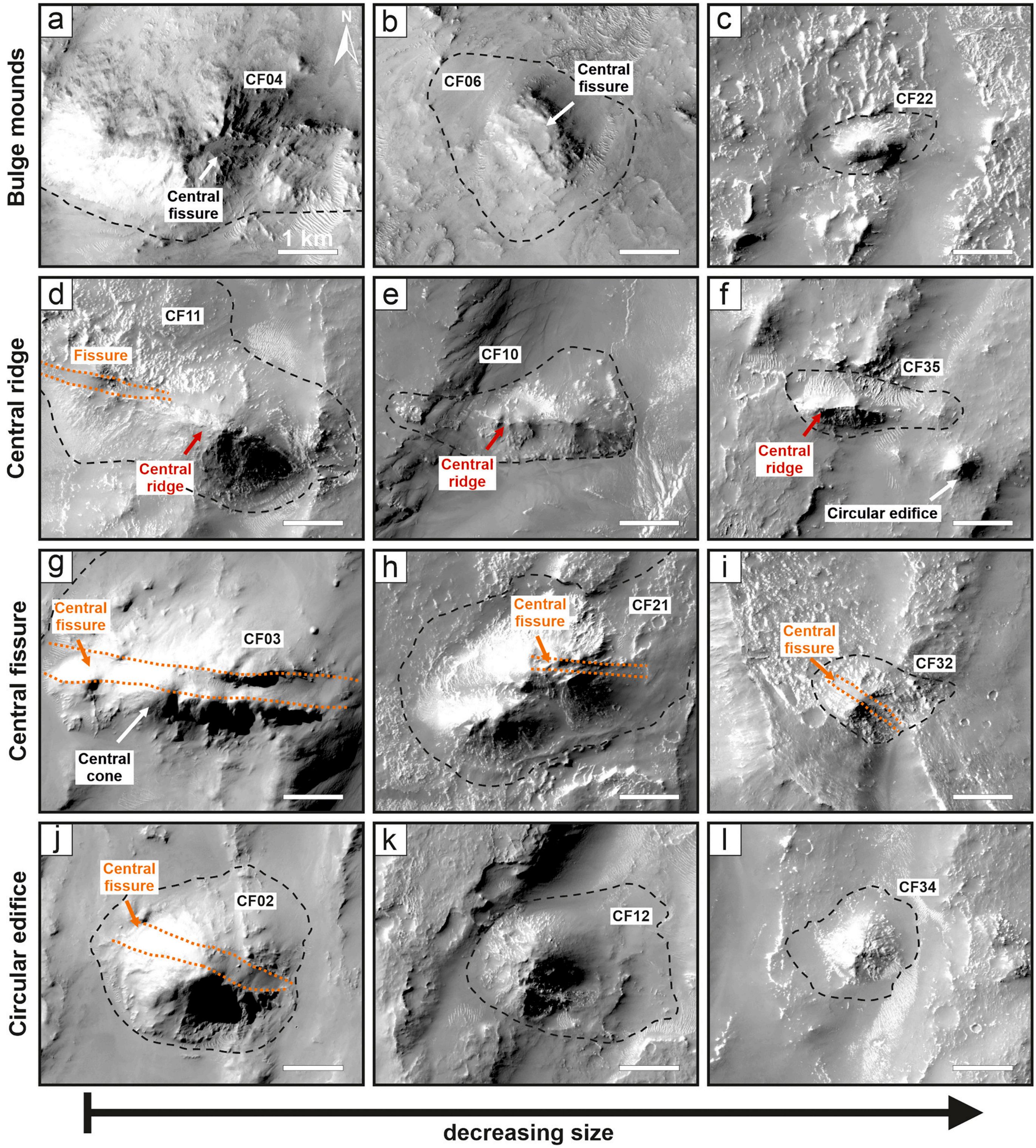

Fig. 2. Examples of the mapped mounds as seen by the CTX imagery system (acquired from GeoScience PDS Node). Based on the morphological features, the investigated mounds might be grouped into four classes with decreasing size including bulge mounds **(a-c)**, mounds with a central ridge **(d-f)**, mounds with central fissure **(g-i)**, and circular mounds **(j-l)**. Such classification allows us to decipher smaller constructs without clear morphological features. See the main text and Fig. 1 for locations within the studied area. The CTX images details: (a) D08_030177_1509, centered at 29.14°S, 253.55°E; (b) D09_030599_1527, centered at 27.42°S, 251.76°E; (c) D17_033737_1522, centered at 27.86°S, 257.65°E; (d) G17_024955_1524; centered at 27.68°S, 255.07°E; (e) D15_033091_1519, centered at 28.18°S, 254.83°E; (f, k) P18_007945_1532, centered at 26.89°S, 255.27°E; (g, j) B20_017439_1503, centered at 29.84°S, 253.2°E; (h) B20_017307_1506, centered at 29.48°S, 256.86°E; (i, l) G17_024955_1524, centered at 27.68°S, 255.07°E. All images have the scale bar of 1 km and are north-oriented.

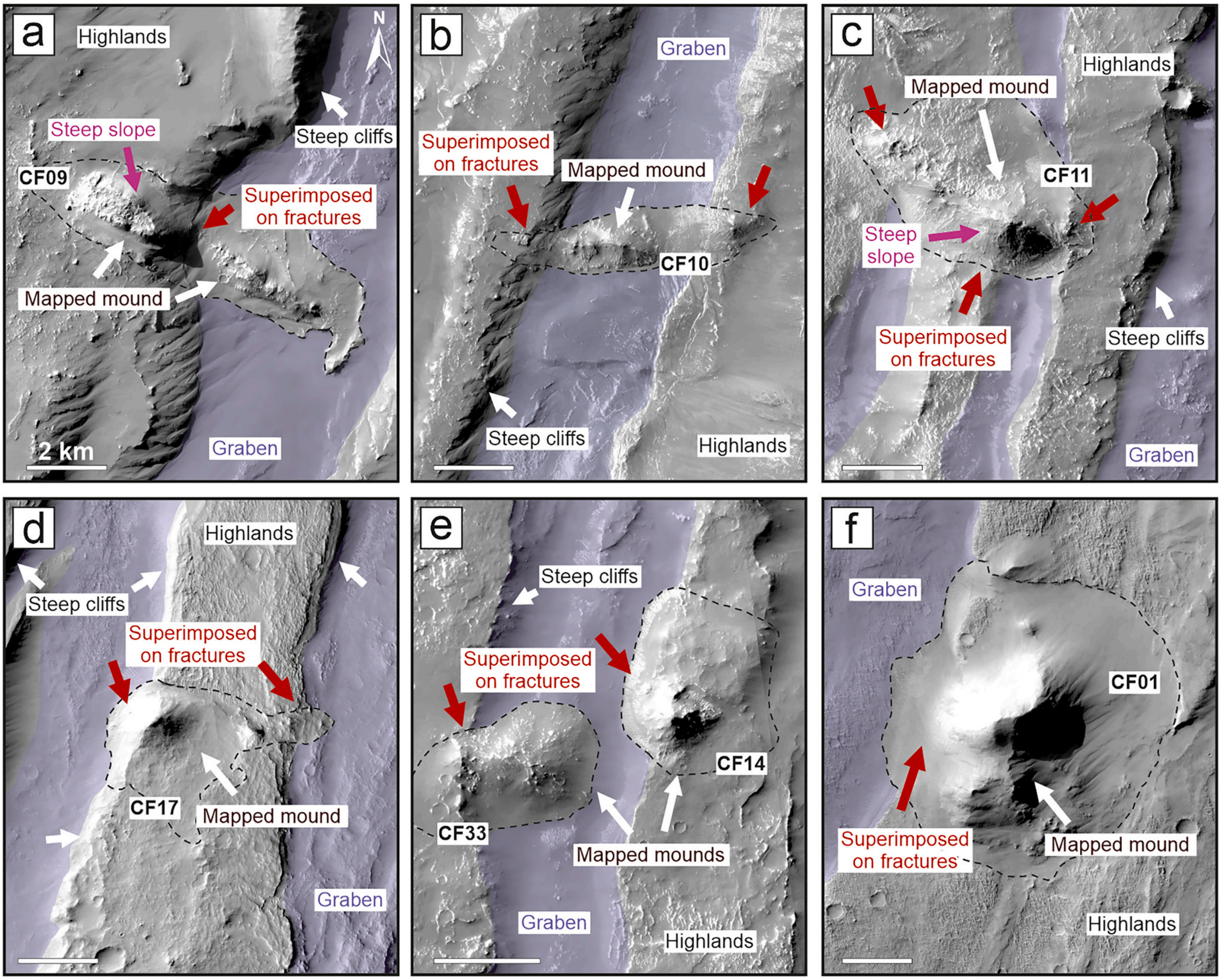

Fig. 3. The structural and stratigraphic relationship between the studied mounds and the fractured terrain of the Thaumasia and Claritas Fossae regions. The studied mounds revealed the constructional character of their formation being superimposed on the fractures bounding the tectonic grabens. Steep slopes of mounds and cliffs indicate negligible erosion and contradict the occurrence of glaciation or aeolian erosion in the study area. **(a-c)** Elongated mounds superimposed on fractures (CTX image P18_008156_1516, centered at 28.54°S, 254.62°E; CTX image G17_024955_1524, centered at 27.68°S, 255.07°E; CTX image D15_033091_1519, centered at 28.18°S, 254.83°E). **(d-f)** Circular- or irregular-shaped mounds whose flanks or deposits are superimposed on fractures (CTX image P18_007945_1532, centered at 26.89°S, 255.27°E; CTX image G17_024955_1524, centered at 27.68°S, 255.07°E; CTX image B21_017650_1537, centered at 26.38°S, 252.19°E). All images have the scale bar of 2 km and are north-oriented.

high concentrations of the LCPINDEX-indicator (Pelkey et al., 2007) highlighted in green on the produced map. To highlight spectral features of interest and reduce systematic artefacts, the numerators were ratioed to bland areas in the same detector columns (denominators), as is typical for CRISM data analysis (Ehlmann et al., 2009; Dapremont and Wray, 2021). This process was conducted using the spectral math toolkits adjusted to the ENVI system. To interpret the obtained mineral spectra, we used the USGS (Clark et al., 2007) and CRISM PDS spectral libraries to compare the obtained spectra with laboratory-derived spectra of pyroxenes.

4. Observations and results

4.1. Morphological characteristics of the Claritas landforms

In the Claritas Fossae region, we mapped 39 mounds that form positive topographic landforms relative to the surrounding terrains. They are spread over an area of 170 × 450 km and include 15 mounds located within the floor of the large Thaumasia graben and 24 mounds in the highlands of Claritas Fossae (Fig. 1c). All of the mapped mounds are observed on the fractured crust extending from the western part of Thaumasia graben, which is partially buried under younger lava flow units, to the eastern region of fractured highlands of Claritas Fossae. We did not find any mounds on the younger lava plain units surrounding the Claritas Fossae region despite a dedicated search campaign. The main clustering of the mounds occurs in the western and central parts of the studied region, characterized by a higher density of fractures, with widely spread individual mounds in the north and east (see Fig. 1c for the detailed spatial distribution of the mounds). Clustering is also visible for individual mounds as they form small groups (e.g., CF09–12, or CF23–25; Fig. 1c), in which mounds are aligned along E-W to NW-SE directions (N090E and N134E with an average value of N111E; see Table 2 for details).

Among 39 of the mapped mounds, we observed diverse morphological features allowing us to group the mounds into sets characterized by the similar appearance in various size ranges (Fig. 2). In plan view,

Table 2
The geographic coordinates and morphological parameters of the mapped mounds in the Claritas Fossae study area. Positions for each mound are shown in Fig. 1.

ID	X coordinate	Y coordinate	Class[1]	HiRISE/ CRISM[2]	Shape[3]	Imagery System[4]	L_{CO} [km]	W_{CO} [km]	A_{CO} [km^2]	H_{CO} [m]	H_{CR} [m]	H [m]	Mean slope [°]	Max. slope [°]	Volume [km^3][5]	Orientation [°]
1	252.171°E	27.292°S	R	H	C	MOLA-HRSC	8.66	6.83	54.25	4195	4854	659	–	–	11.92	n/d
2	252.826°E	27.613°S	R	H/C	C	MOLA-HRSC	2.88	2.72	7.33	4501	4804	303	–	–	0.74	109.7
3	252.929°E	27.593°S	R	C	E	MOLA-HRSC	4.72	3.39	21.48	4489	4803	314	–	–	2.25	95.7
4	253.315°E	27.395°S	R	n/a	E	MOLA-HRSC	6.02	3.98	24.92	4494	5119	625	–	–	5.19	100.8
5	251.848°E	27.818°S	R	n/a	E	CTX	2.99	1.81	10.52	4474	4767	293	7.9	36.5	0.82	127.3
6	251.894°E	27.864°S	R	n/a	E	CTX	1.84	1.43	9.95	4444	4657	213	7.6	38.2	0.70	130.7
7	252.058°E	28.073°S	R	n/a	E	MOLA-HRSC	2.20	0.91	2.03	n/a	n/a	n/a	–	–	n/a	n/d
8	251.794°E	28.460°S	R	n/a	C	CTX	2.18	2.20	10.73	4691	4947	256	8.2	38.0	0.96	130.3
9	254.522°E	28.283°S	R	H tar./C	E	MOLA-HRSC	3.17	1.96	6.86	4074	4363	289	–	–	0.66	118
10	254.920°E	28.081°S	R	n/a	E	MOLA-HRSC	2.57	1.30	3.78	4157	4301	144	–	–	0.18	95.6
11	255.199°E	28.629°S	R	H tar.	E	MOLA-HRSC	4.27	2.77	8.97	6675	7201	526	–	–	1.57	110.4
12	255.398°E	28.728°S	R	H tar.	C	CTX	1.99	1.91	3.84	6286	6555	269	10.1	46.5	0.50	n/d
13	255.457°E	28.713°S	R	H tar.	C	CTX	2.35	2.14	7.40	6170	6526	356	10.3	36.8	1.00	n/d
14	255.263°E	28.374°S	R	n/a	C	MOLA-HRSC	2.09	2.03	4.47	6402	6695	293	–	–	0.44	n/d
15	255.325°E	28.072°S	R	H tar.	C	CTX	2.11	1.98	4.62	6540	6826	286	11.0	32.0	0.59	124.4
16	255.270°E	28.022°S	R	H tar.	E	MOLA-HRSC	3.05	1.61	2.83	6659	6993	334	–	–	0.32	128
17	255.558°E	27.898°S	R	n/a	C	MOLA-HRSC	2.35	2.14	4.09	6000	6308	308	–	–	0.42	n/d
18	255.380°E	27.550°S	R	n/a	E	CTX	1.99	0.94	5.66	5986	6183	197	6.4	32.3	0.41	n/d
19	255.205°E	26.113°S	R	n/a	E	MOLA-HRSC	7.56	4.31	56.19	5739	6629	890	–	–	16.67	n/d
20	255.998°E	28.310°S	R	n/a	E	MOLA-HRSC	5.49	3.10	22.58	6225	6812	587	–	–	4.42	n/d
21	256.752°E	28.378°S	R	n/a	E	CTX	3.52	2.27	11.64	6354	6708	354	10.9	36.1	1.42	91.2
22	257.615°E	27.679°S	R	n/a	E	MOLA-HRSC	1.19	0.79	1.40	n/a	n/a	n/a	–	–	n/a	90.5
23	259.702°E	28.240°S	R	n/a	E	MOLA-HRSC	2.59	1.75	3.91	7367	7534	167	–	–	0.22	n/d
24	260.082°E	28.420°S	R	H/C	C	CTX	3.93	3.67	19.81	6759	7690	931	14.0	42.1	9.39	n/d
25	260.260°E	28.531°S	R	H	C	CTX	3.97	3.68	11.81	7024	8011	987	18.3	37.1	5.62	n/d
26	252.662°E	27.387°S	I	n/a	C	MOLA-HRSC	1.53	1.18	1.54	n/a	n/a	n/a	–	–	n/a	n/d
27	251.925°E	27.915°S	I	n/a	E	MOLA-HRSC	1.66	0.78	1.45	n/a	n/a	n/a	–	–	n/a	133.8
28	252.083°E	28.127°S	I	n/a	E	MOLA-HRSC	1.01	0.68	0.75	n/a	n/a	n/a	–	–	n/a	n/d
29	253.556°E	27.506°S	I	n/a	E	MOLA-HRSC	3.72	2.03	7.76	4375	4635	260	–	–	0.67	110.3
30	254.052°E	28.150°S	I	n/a	C	MOLA-HRSC	2.17	1.99	4.94	4471	4630	159	–	–	0.26	n/d
31	254.986°E	28.444°S	I	n/a	E	MOLA-HRSC	2.11	0.88	1.78	n/a	n/a	n/a	–	–	n/a	95.4
32	255.184°E	28.830°S	I	n/a	E	MOLA-HRSC	1.35	1.04	1.30	n/a	n/a	n/a	–	–	n/a	n/d
33	255.206°E	28.386°S	I	n/a	E	MOLA-HRSC	2.67	1.97	4.44	6482	6687	205	–	–	0.30	90.6
34	255.219°E	27.970°S	I	n/a	C	MOLA-HRSC	1.39	1.35	1.37	6263	6445	213	–	–	0.10	n/d
35	255.539°E	28.457°S	I	n/a	E	MOLA-HRSC	1.67	0.76	0.92	n/a	n/a	n/a	–	–	n/a	91.7
36	255.621°E	28.396°S	I	n/a	E	MOLA-HRSC	1.49	0.57	0.45	n/a	n/a	n/a	–	–	n/a	94.1
37	255.860°E	28.377°S	I	n/a	E	MOLA-HRSC	2.20	0.77	1.29	6008	6088	80	–	–	0.03	129.1
38	256.529°E	27.936°S	I	n/a	C	HRSC	4.66	4.18	45.81	6076	6637	561	6.1	26.4	9.10	123.5
39	256.834°E	27.884°S	I	H/C	E	HRSC	11.84	5.63	111.24	6005	7144	1139	8.4	18.9	55.83	n/d

L_{CO} – the basal length measured as a longer axis of the mound; W_{CO} – the basal width of the mound measured perpendicular to the elongation; A_{CO} – the area of the mound basement; H_{CO} - the absolute basal mound height; H_{CR} – the absolute height of the summit crater; H – the relative height of the mound (the difference between H_{CR} and H_{CO}). The slopes have been calculated based on the CTX-based DEM applying an automated tool of the ArcGIS software.

[1] R – recognized; I – inferred;

[2] H – HiRISE image available; H tar. – HiRISE image targeted; C – CRISM data available;

[3] C – circular; E – elongated;

[4] MOLA-HRSC - blend of digital elevation model (DEM; 200 m/px; Fergason et al., 2018) derived from the Mars Orbiter Laser Altimeter (MOLA) and High-Resolution Stereo Camera (HRSC), CTX – DEM derived from the CTX stereo pairs; HRSC – DEM derived from the High-Resolution Stereo Camera (HRSC).

[5] For MOLA-HRSC DEM the volume has been measured using the equation for the frustum, whereas the volume for edifices targeted by CTX- and HRSC-based DEM has been calculated using the ArcGIS software applying an automated tool calculating the volume above the reference height set in this study as H_{CO}.

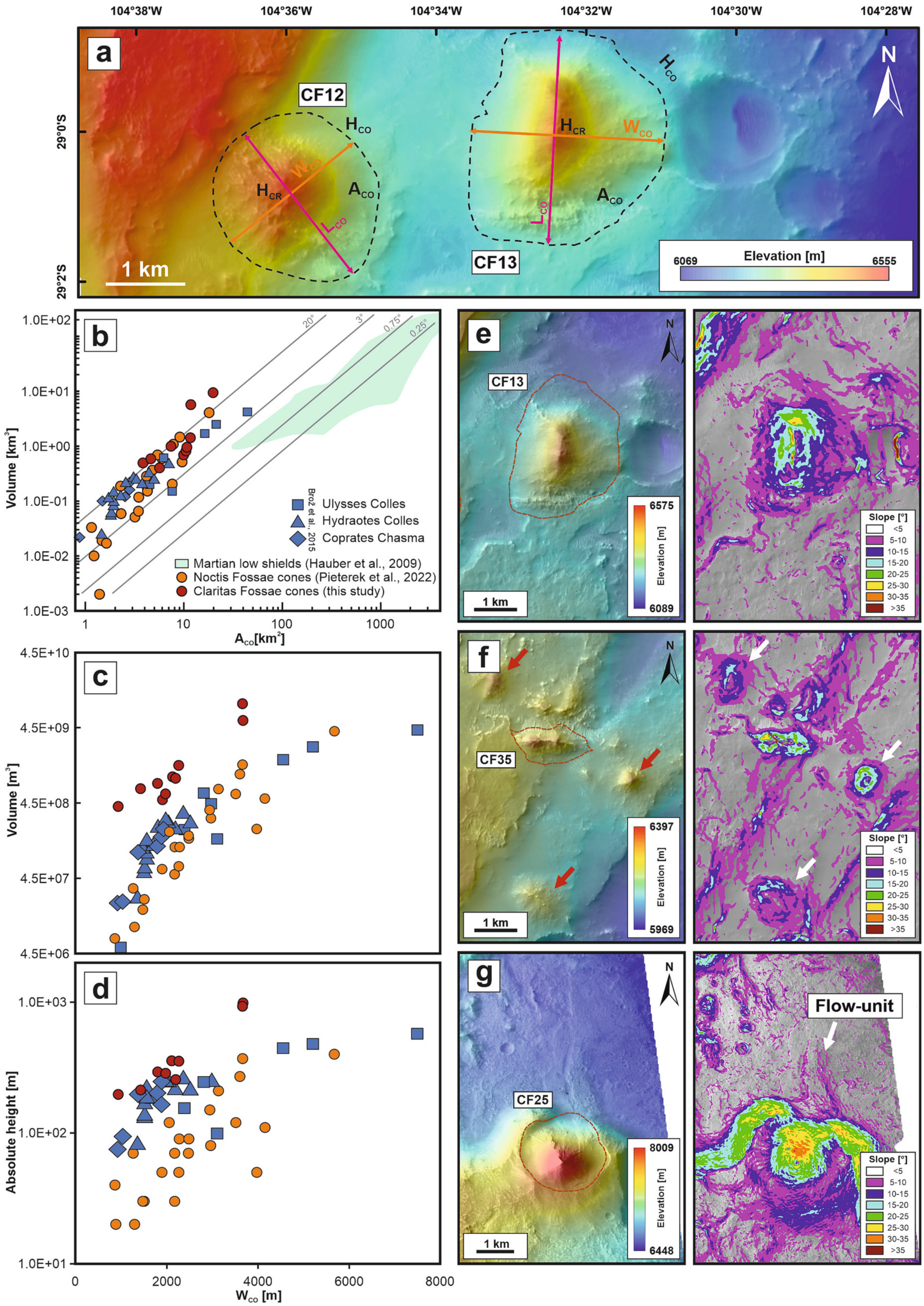

(caption on next page)

Fig. 4. **(a)** Digital elevation model (DEM) derived from a CTX-based stereo pair (P18_007945_1532 and N10_066414_1533; for detail see Table 1) of two mounds (CF12–13) showing the morphological parameters measured in this study. Histograms **(b-d)** presenting morphological parameters of the Claritas Fossae mounds. The obtained results were compared to low-shield volcanoes analyzed in the Tharsis Volcanic Province (Hauber et al., 2009) (b) and scoria cones from Ulysses Colles, Hydraotes Colles, Coprates Chasma volcanic fields (Brož et al., 2015) as well as Noctis Fossae (Pieterek et al., 2022b) (panels b-d). **(e-g)** Topographic maps of the selected mounds (marked by red dashed lines) and corresponding slope maps determined using the Slope Analysis tool in the 3D Analyst ArcToolbox of ArcMap software. The red arrows in panel f pinpoint the landforms that resemble the mapped mounds, however, their classification might be too speculative due to their sizes. The areas with slope values <5°are transparent. Moreover, on the slope map of panel g, the boundaries of the north-trending flow unit originating from CF25 are well established. (e and f) Digital elevation model (DEM) derived from the CTX-based stereo pairs (P18_007945_1532 and N10_066414_1533). (g) DEM derived from the CTX-based stereo pairs (P13_005954_1529 and K15_059095_1529). More detailed information about CTX-based DEMs is presented in Table 1. (For interpretation of the references to colour in this figure legend, the reader is referred to the web version of this article.)

the morphology of studied mounds, in general, is characterized by elongated to irregular or, more rarely, circular outlines and relatively steep-appearing flanks. The detailed morphology of the mounds varies as some mounds reveal central ridges (Fig. 2d-f), central fissures (Fig. 2a-c and g-i), or central summits (Fig. 2k-l). In most cases, the flank surfaces of the mounds display a blocky texture (Fig. 2c-f, h-l), however, sometimes aeolian deposits can be observed, especially at the base of the mounds (Figs. 2g and 3f). With one exception (CF25), the studied mounds do not show flow units emanating from their summits or flanks and form edifices with well-defined basal outlines (Figs. 2–3). All mounds are superimposed on older fractured terrain, thus the mounds postdate the N-S fracturing event (Fig. 3). For example, elongated

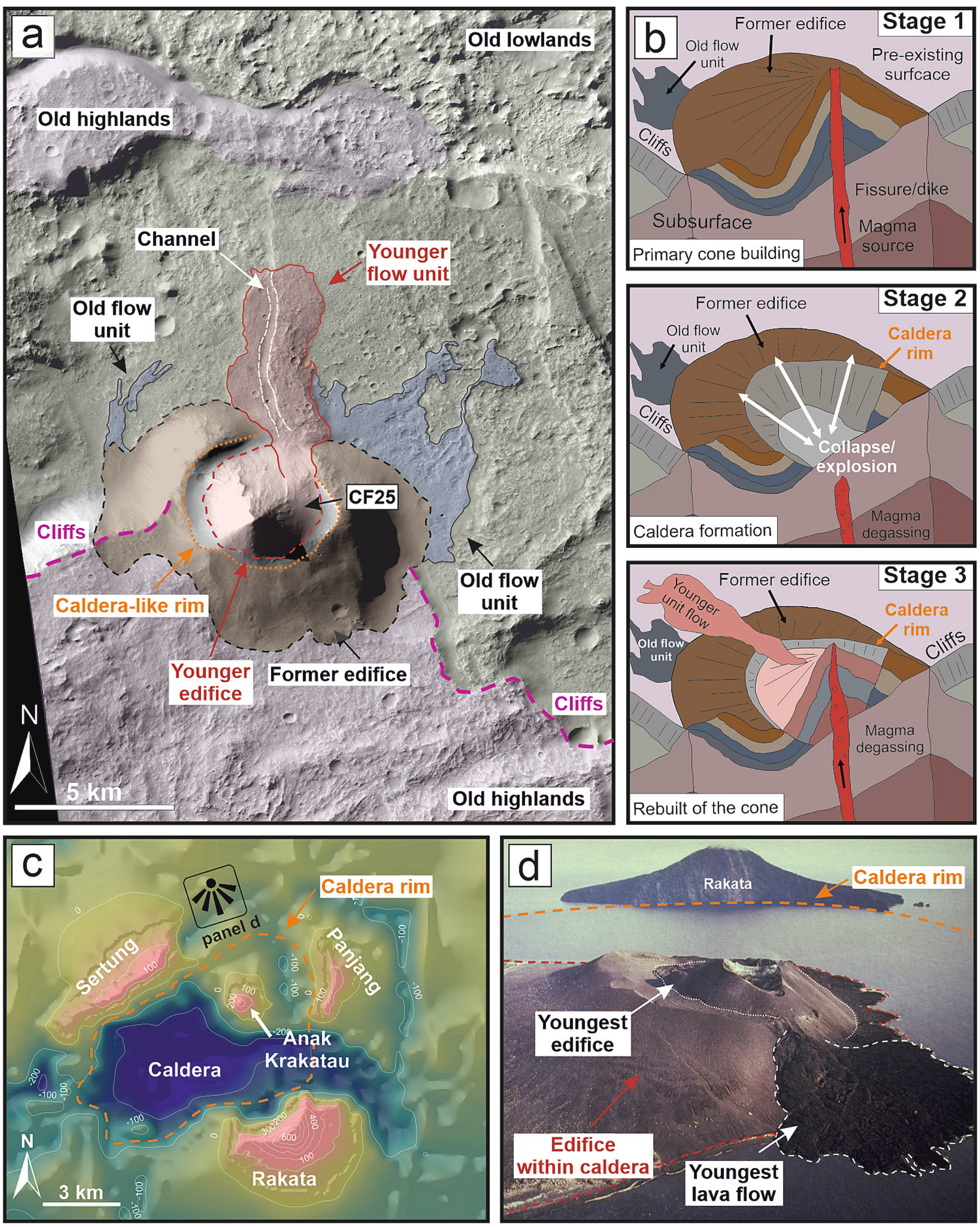

Fig. 5. **(a)** Schematic drawing showing the simplified map explaining the formation of the nested central cone (CF25) surrounded by the elevated caldera-like rim. The central circular edifice is highlighted by smooth slopes compared to the surrounding terrains and the flow unit originated from the northern slope. CTX image B22_018098_1519, centered at 28.2°S, 260.23°E. **(b)** Three stages of development of the depicted nested cone in the plan-map view with the magma source as feeder dike that is depicted in the cross-section. **(c)** Terrestrial example of the post-caldera edifice (Anak Krakatau volcano; first emerged from the sea in 1929) with the submarine caldera that was formed after the Krakatau eruption in 1883. The caldera rim is highlighted by three truncated islands. The bathymetry data were downloaded from the GMRT database. The location of the photo presented on panel (d) is highlighted. **(d)** Photo of the Anak Krakatau volcano that is volcanically active with well-distinguishable volcanic features. Image credit: Volcanological Survey of Indonesia.

mounds superpose the N-S-trending grabens (Fig. 3a-e) and the mound-associated deposits cover the bounding slopes and floors of the grabens (Fig. 3d–f) as well as the former highland terrains (Fig. 3f).

Basal lengths and widths of the mounds range from 1.0 to 11.8 km with an average value of 3.2 km and from 0.6 to 6.8 km with an average value of 2.2 km, respectively. The basal areas range from 0.5 up to 111.2 km^2 with an average value of 13.0 km^2 and a median value of 4.9 km^2 (Table 2 and Fig. 4). The largest landform (CF39) reveals a complex structure comprising of several elevated blocks along a main W-E oriented ridge. The CTX-based topographic data for the targeted mounds (10) show that these landforms are characterized by relative heights ranging from ~200 to ~990 m with a median value of ~290 m (Table 2 and Fig. 4b). Using the determined morphological parameters, we calculated volumes ranging from 0.4 to 9.4 km^3 with an average value of 2.1 km^3 and a median value of 0.9 km^3 (based on 10 mounds, for details see Table 2 and Fig. 4a). The high-resolution CTX-based DEMs allow us to calculate the slopes that reveal mean values for individual mounds ranging from 6.4° to 18.3° (Table 2), but the maximum values can reach up to ~40°, significantly exceeding the angle of repose of ~30–35° (Kleinhans et al., 2011; Atwood-Stone and McEwen, 2013). However, these values are related to scarps and cliffs that sometimes occur locally on the flanks of the studied mounds due to the blocky structure of the mounds and do not represent values for their mean slopes (Fig. 4).

In the eastern part of the study region, we mapped three mounds (CF23–CF25) aligned in the WNW direction (Fig. 1). The easternmost mound (CF25) is located at the cliff that locally separates a southern elevated region from a northern lowered terrains (for local geological context see Figs. 5a and 6a) and it comprises a caldera-like rim partly infilled by a conical landform. The caldera-like rim is characterized by a circular plan view shape with a diameter of ~5 km, whereas the internal mound has ~3 km diameter at its base. The caldera-like rim raises ~680 m above its surroundings (~6620 m above the datum) to its highest point, with slopes of ~18° (Figs. 4g and 7). The conical mound situated inside the caldera-like rim has ~610 m in height and mean slopes of ~24° (Fig. 4). A HiRISE image (ESP_076556_1510; Table 1) reveals that the central cone is composed by material disintegrating into meter-sized boulders (Fig. 6b). On the lowland terrain, older flow units can be distinguished, characterized by irregular boundaries, being partially covered by the material of the caldera-like rim (Fig. 6c–d) that now constitutes the remnants of the primary mound. In the northern part of the mound, the caldera-like rim is breached by a younger flow unit which is ~5 km in length. Based on the high-resolution DEM, the flow

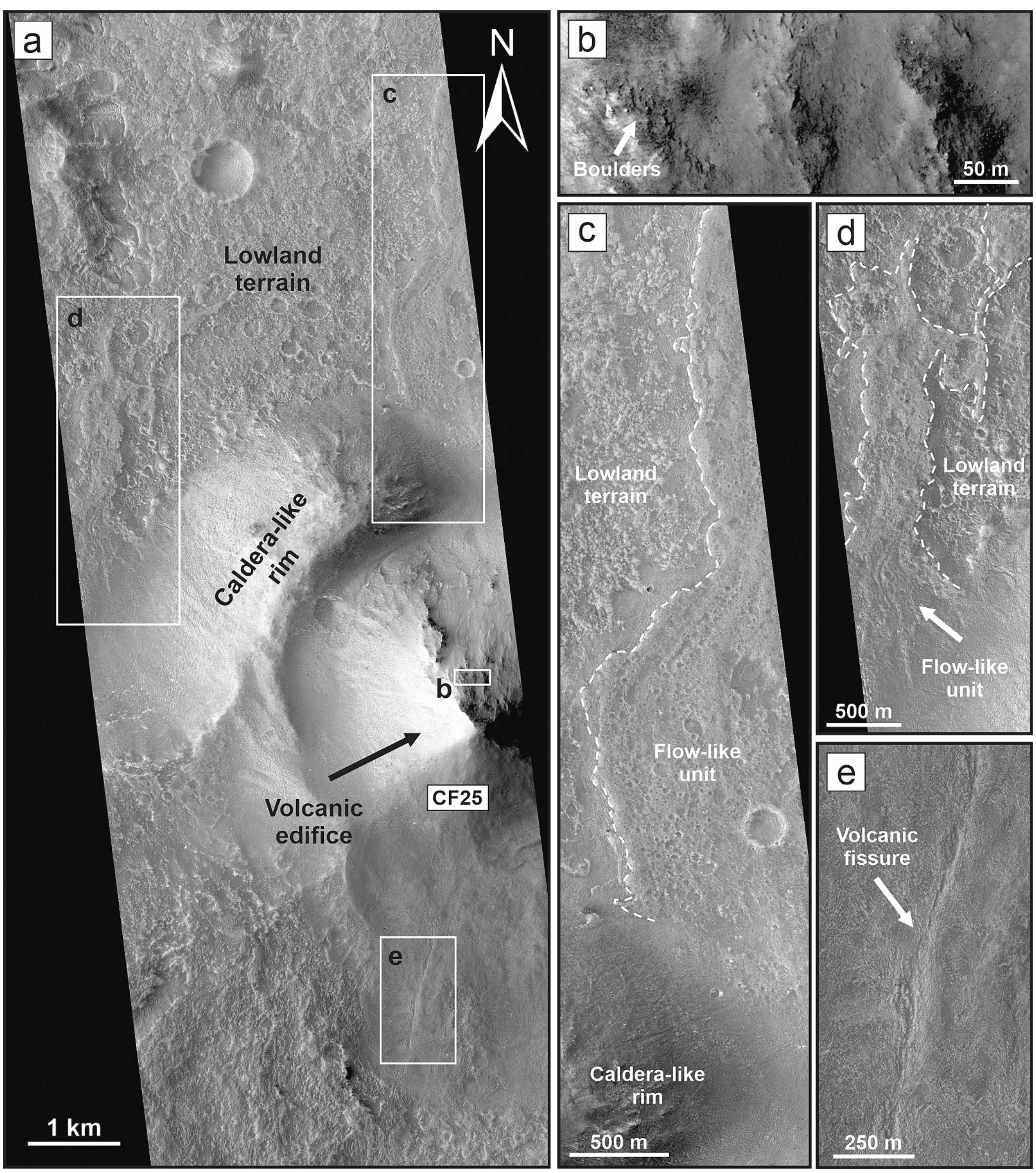

Fig. 6. An overview image **(a)** of the cone CF25 with associated flow-like units (HiRISE image ESP_076556_1510, centered at 28.521°S, 260.223°E). **(b)** Close-up image of the northern slope of the cone showing the presence of boulders associated with hard rock exposures. **(c)** The northern flow-like unit that likely originate from the central cone (Fig. 5) with well-distinguishable boundary (white dashed line). **(d)** The eastern flow-like unit with irregular boundaries (white dashed lines) that probable originate from the initial effusive eruption that predates the central edifice collapse and further rebuilt. **(e)** The close-up image of the putative volcanic fissure that is emplaced in the southern part of the volcanic edifice. The material likely expelled from the fissure cover the rough surface of highland terrain indicating its younger origin.

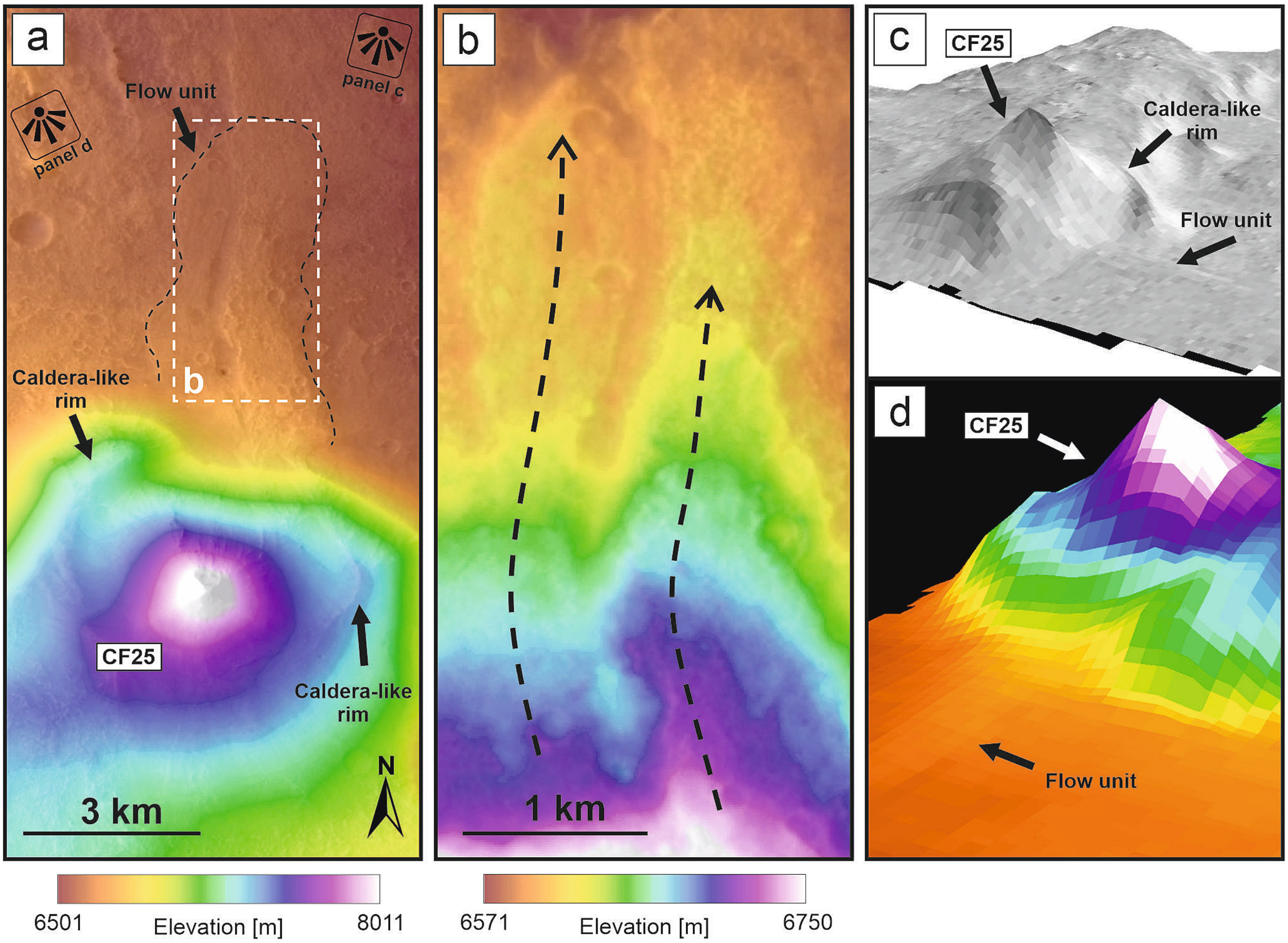

Fig. 7. **(a)** Digital elevation model (DEM) derived from the CTX-based stereo pairs (P13_005954_1529 and K15_059095_1529; for detail see Table 1) underlined by the CTX image (P13_005954_1529) of the cone CF25 showing the morphological features characteristic for putative volcanic construct including caldera-like rim and associated flow unit. The zoom-in image **(b)** on the north-trending flow unit likely originates from the central cone. The DEM shows the decreasing elevation toward the north indicating the flow structure. **(c & d)** 3D visualizations of the CF25 edifice using the CTX-based DEM with a distinctive flow-unit that is elevated compared to the surrounding lowlands. These visualizations are 3 times exaggerated.

unit begins at the central part of the internal conical-shaped mound and extends northwards being channelized into two streams, covering the lowland terrains, with an elongated central depression characterized by widths that range from 180 to 360 m (Figs. 5a and 7). In addition, another flow-unit feature, however less visible, is present on the southern slopes that cover the rough surface of the highland terrain. A HiRISE image (ESP_076556_1510) of this area reveals the presence of a fissure-like feature associated with the southern flow unit of the inner mound (Fig. 6e). The entire structure is characterized by a smoother surface when compared with the surrounding terrain.

4.2. CRISM analysis of the Claritas mounds

Only one CRISM image (HRS00012172; Fig. 8) completely covers two studied mounds (CF02–03), whereas three other CRISM images partially cover flanks or surroundings of some other mounds (CF09, 24, and 39) in the central and eastern part of the investigated region (Fig. 9). The two completely covered mounds (CF02–03; Fig. 8a) reveal extremely high LCPINDEX values (Pelkey et al., 2007; Viviano-Beck et al., 2014) indicative of possible low-calcium pyroxenes. That index, highlighted in green in Fig. 8, is particularly distinct along the central fissures (Fig. 8b). The regions of interest within the green areas show a distinct absorption at ~0.9 μm (Fig. 10) and a broad absorption at ~1.9 μm (Fig. 8c). Both absorptions support a mineralogical composition dominated by LCP. Furthermore, the comparison of the obtained spectra with spectra of terrestrial reference samples measured in the laboratory highlights the spectral similarity with LCP (Figs. 10c and 11d). The CF09 mound (Fig. 3a) shows different morphological characteristics compared to the CF02–03 mounds. It forms an elongated construct with a blocky summit plateau and steep-appearing flanks covered by boulders (Fig. 12e–g) which northern parts were covered by the spectral data of CRISM. The CF39 mound situated at the Claritas Fossae highlands (Fig. 1c), being the largest of the mapped mounds (Table 2), is characterized by several elevated blocks and ridges which were also targeted by CRISM. Moreover, in the easternmost part of the Claritas Fossae, in the vicinity of the mapped mound CF24, the CRISM spectral summary browse image (comprising D2300, LCPINDEX2, and HCPINDEX2 products) showed that the rough surface with a small mound (< 1 km along the long axis) is characterized by intense green colour (Fig. 9d). Again, in all these cases, the LCP are spatially associated either with the flanks of the mounds (Fig. 9b–c) or elevated landforms close to the mounds (Fig. 9d). The spectral signatures extracted for selected regions of interest on these sites (Fig. 9b–d) exhibit a broad absorption at ~1.9 μm in the spectral ratio (Fig. 11a–c) similar to those previously described for CF02–03 (Fig. 8c).

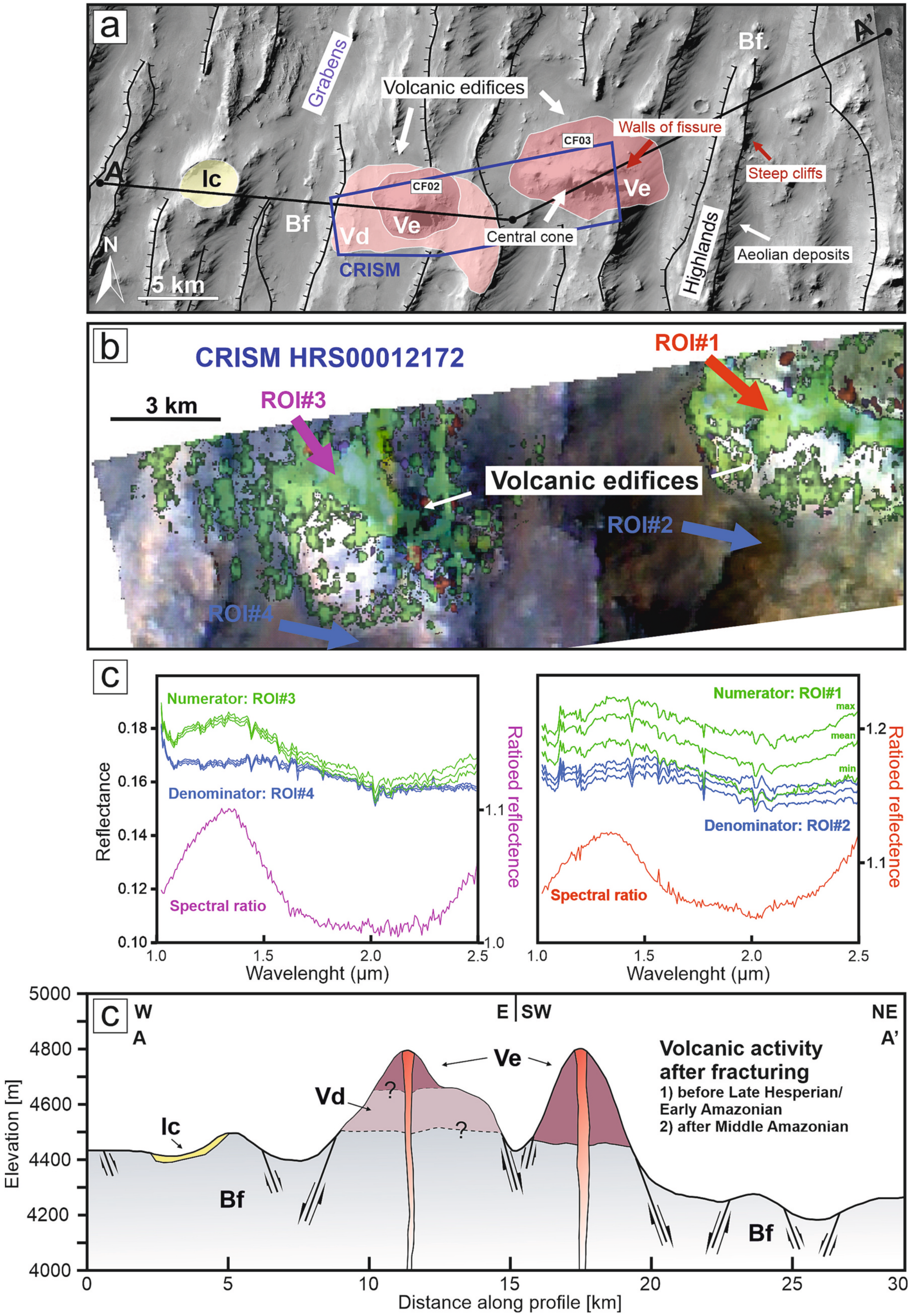

(caption on next page)

Fig. 8. Evidence supporting the hypothesis of the volcanic origin of the studied mounds in the Claritas Fossae region. **(a)** An overview map showing two LCP-rich edifices (CF02 and 03) with central fissures superimposed on the fractured terrain that were targeted by the CRISM instrument. The blue insert shows the location of the analyzed CRISM data. CTX image B20_017439_1503, centered at 29.84°S, 253.2°E. **(b)** The enhanced visible colour image of the studied edifices overlapped with the IR-derived custom product image (R: D2300, −0.00495–0.00946; G: LCPINDEX2, 0.02260–0.03002; B: HCPINDEX2, 0.02257–0.03735). CRISM image HRS00012172, centered at 27.6385°S, 252.8634°E. The green colours are spatially associated with the volcanic edifices, especially with the central fissure, indicating a LCP-rich composition. All images are north-oriented. **(c)** Plots showing spectral characteristics of the studied edifices (CF02 and 03) and their averages (ROI#1 = 66 px; ROI#2 = 15 px; ROI#3 = 24 px; ROI#4 = 12 px) of nominator (green) and denominator (blue) from locations indicated by the corresponding arrows in panel (b). Please note that we included the min, max and mean spectrum for the regions of interest to show the consistency of the spectral signature throughout these regions. In both panels, the vertical scale of reflectance is scaled the same. Below, we present the corresponding cross-section **(d)** showing actual geological context. Units: Ve – volcanic edifice; Vd – volcanic deposits; Bf – fractured terrain; Ic – impact crater. Black lines with hatches on one side indicate grabens dipping toward the hatched side. The cross-section elevation model is based on a blend of digital elevation model (200 m/px; Fergason et al., 2018) data derived from the Mars Orbiter Laser Altimeter (MOLA) and High-Resolution Stereo Camera (HRSC). (For interpretation of the references to colour in this figure legend, the reader is referred to the web version of this article.)

5. Discussion

5.1. Origin of the Claritas mounds

In this study, we identified 39 mounds (Figs. 2–4) that form positive topographic landforms superimposed on the Noachian-age terrains both of the Thaumasia graben and the Claritas Fossae highlands characterized by a long-lasting tectonic deformation history (Fig. 1). As the walls of the main N-S-trending fractures are covered by the mound-associated deposits (Figs. 3 and 11b), this implies that the mounds postdate the fracturing itself and that their formation could have been controlled by the pre-existing fractures. Such structural relationship between younger edifices and older, fractured crust has been observed for some other putative Martian volcanic fields, including Ulysses Colles (Brož and Hauber, 2012) and Noctis Fossae (Pieterek et al., 2022b), as well as is common for volcanic edifices in Iceland or in the Ethiopian rift (Fig. 13a; Opheim and Gudmundsson, 1989; Korme et al., 1997; Corazzato and Tibaldi, 2006; Hjartardóttir et al., 2016; Tibaldi et al., 2017). Fractured terrains represent weak crustal zones that enable the migration of magma (or other fluids) from source regions to the surface (Lesti et al., 2008; Le Corvec et al., 2013; De Toffoli et al., 2018). At the same time, we conclude that the studied mounds have been formed by aggradational rather than degradational processes as many of the studied mounds display steep scarps bordering their central fissures (Figs. 2, 12a-c, 14c-d). Such morphology is inconsistent with an origin as erosive remnants as the erosion would lead to topographic degradation and morphologic smoothening. In addition to the mounds, grabens also exhibit steep walls that are without any evidence of boulders at the foot of the walls. This suggests a negligible effect of erosional processes in the studied region starting from the graben formation in the Hesperian period until today (Fig. 3). Therefore, we assert that the formation of the mounds must be related to the extrusion of material from the subsurface.

Previous studies showed that material extruded to the surface of Mars was most commonly magma (Wilson and Head, 1994; Wilson, 2009; Peters et al., 2021), or less frequently mud, a mixture of water and sediments (e.g., Komatsu et al., 2016; Cuřín et al., 2023; or see Brož et al., 2023 and references therein for an overview). Therefore, sedimentary volcanism should be considered as a plausible option for the formation of the studied mounds. It was shown that in contrast to igneous volcanism, sedimentary volcanism on Mars is restricted to specific locations where favorable conditions were present in the past. Specifically, these are areas where (1) a relatively quick accumulation of sufficiently thick sedimentary deposits occurred, (2) some strata of fine-grained sediments mixed with liquid water formed within these deposits, and (3) the sediments have been overpressured or experienced gravitational instability to trigger fluid expulsion (Brož et al., 2023 and references therein). As the studied field is situated on a highland belt consisting of a heavily fractured crust, the existence of a stable aquifer or other sources of mud is highly unlikely. Moreover, given the tectonic-volcanological evolution of Tharsis, it is unlikely that a continuous layer of fine-grained deposits capable of holding a large quantity of water would be buried in the subsurface. Therefore, the mapped mounds cannot be easily associated with the process of subsurface sediment mobilization suggested to operate in other areas with more favorable context as within basin floors (Okubo, 2016) or in the northern Planitiae (Komatsu et al., 2016; Brož et al., 2019; Dapremont and Wray, 2021). Hence an explanation in terms of igneous volcanism is more plausible given the geological context.

The following morphological characteristics of the studied mounds also suggest their volcanic origin: (1) the regional alignment of the mounds indicating common supplying dike(s) similar to terrestrial volcanic systems (Fig. 1); (2) the presence of central fissures (Fig. 2); (3) the slopes' surfaces and ridge-structures indicating rock exposures rather than fine-grained loose material (Figs. 3 and 12); and (4) morphological similarities (e.g., basal area, absolute height, and slope) with other Martian small-scale volcanoes (Fig. 4).

The studied mounds are aligned and elongated in a WNW-ESE direction (Table 2). In addition, a cluster of mounds (CF09–12; Fig. 1) located close to the bounding fault, might have been formed due to a common volcanic event, as each one of the mounds reveals a similar appearance and likely represents a protruding dike. In this particular case, the CF09 mound comprises two constructs emplaced both within the graben and on the highland terrain (Figs. 3a and 12d). Although they are separated by the wall of the graben, they might be sourced by a common supplying dike as it was observed during the Fagradalsfjall eruption (Phase 2; April 2021) in Iceland (Barsotti et al., 2023) due to the small difference in elevation between vents. On Earth, the magma chamber and tectonic stress mainly control the dike emplacement that, in turn, controls the location and geometry of vents and volcanoes (e.g., Annen et al., 2001; Tibaldi et al., 2017). Numerical modelling conducted by Annen et al. (2001) shows that terrestrial volcanic edifices tend to be high with steep flanks when the feeder dikes are thick and migrated from a small and shallow magma chamber(s) and if the magma has high yield strength that depends on the composition (see Section 5.3 for details). In that case, the elongations of volcanic edifices are directly related to the trend of subsurface dike(s) and express the tectonic-scale stress regime of their extensional settings (Acocella and Neri, 2009; Paulsen and Wilson, 2010). This might be the case for our study area as the mapped mounds reveal E-W to NW-SE elongations (Table 2) being in agreement with the NW-SE-trending ridges (Fig. 1; Hauber and Kronberg, 2005). On Mars, dike-controlling scenarios for volcanic edifices have already been proposed to explain the formation of distributed volcanoes within Tharsis (Pieterek et al., 2022a), and even of small-scale volcanoes in Noctis Fossae (Pieterek et al., 2022b). In addition to the mound elongations, we demonstrated that some of the studied mounds display well-preserved central fissures that sometimes dissect the entire mound (Figs. 2g–j and 14) and are probably the surface manifestation of subsurface dike(s). These morphological features are similar to terrestrial multiple rifted cones that, e.g., have been described on the Etna's flanks (Corazzato and Tibaldi, 2006) or dissected cones in the Main Ethiopian Rift (Hunt et al., 2020).

The morphology and shape of the studied mounds in most cases are consistent with those of terrestrial volcanic edifices (for example, edifices located in Iceland, Hawaii, or Ethiopia), with one important

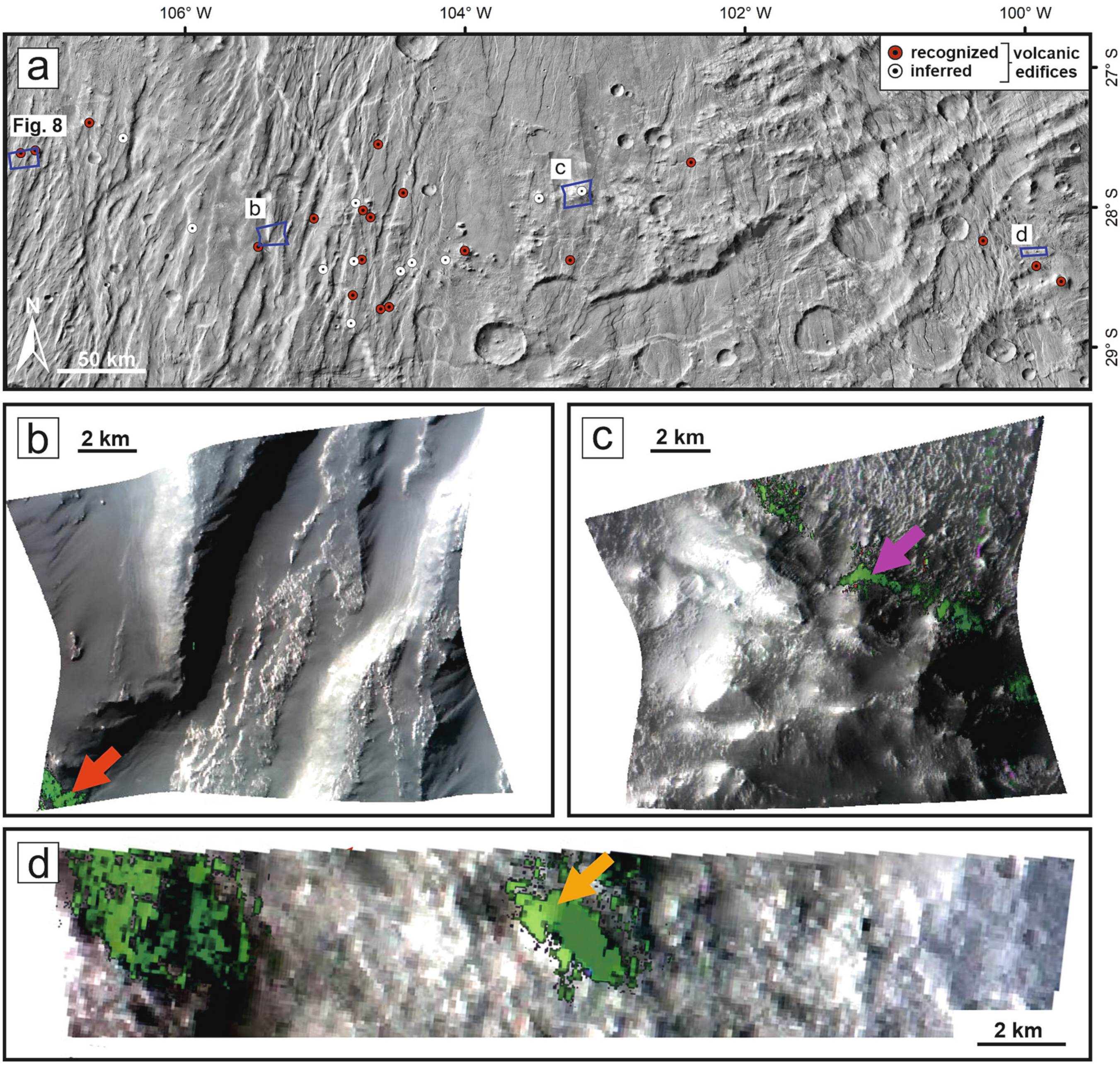

Fig. 9. Association between studied edifices and the distribution of LCP. **(a)** An overview image showing the distribution of available CRISM (marked by blue rectangles) data within the studied area. The distribution of the mapped edifices is marked by red and white dots that corresponds to Fig. 1. In four cases, the distinguished edifices are fully or partially covered by the CRISM spectral data (see Fig. 6a). **(b-d)** The enhanced visible colour image of the studied edifices overlapped with the IR-derived custom summary product images (R: D2300; G: LCPINDEX2; B: HCPINDEX2). In all panels, the green colour indicates the distribution of LCP that mostly occur on the edifices' slopes. The arrows pinpoint the locations of ratioed spectra presented in Fig. 8. All images are north-oriented. (b) CRISM image FRT0000A91D, centered at 28.2115°S, 254.6396°E. (c) CRISM image FRT0001C5B6, centered at 27.941°S, 256.8343°E. (d) CRISM image HRS000119AF, centered at 28.3556°S, 260.0946°E. (For interpretation of the references to colour in this figure legend, the reader is referred to the web version of this article.)

variation, i.e. terrestrial analogues are smaller (Fig. 13). Such discrepancy in size might be explained by considerations provided by Wilson and Head (1994) who highlighted that the dikes and volumes of erupted material should be larger on Mars due to the lower gravity. We also conducted a comparative analysis of the morphological parameters of the studied mounds (determined only for those mounds targeted by the CTX-based DEMs) with other kilometer-sized volcanic edifices on Mars (Fig. 4). The Claritas Fossae mounds show a similar range of basal areas when compared to other Martian low-volumetric volcanic edifices, whereas they are characterized by larger absolute heights, and hence slightly larger volumes and steeper flanks.

Based on the considerations mentioned above, we concluded that the studied mounds are volcanic in origin and that the majority of them were formed by relatively low-volumetric eruptions. CTX and HiRISE images reveal that the studied mounds often form elongated ridges with blocky textures and meter-size boulders on their slopes (Figs. 2d-f, 12) being consistent with Martian landforms formed by viscous lava flows (Mangold et al., 2010). In addition, such morphologies are commonly present in the case of terrestrial effusive-dominated volcanic edifices (Fink and Anderson, 1999; Gonnermann and Manga, 2003). This indicates that they are formed by rocks (solidified volcanic lava) rather than fine-grained loose deposits whose occurrence is common for

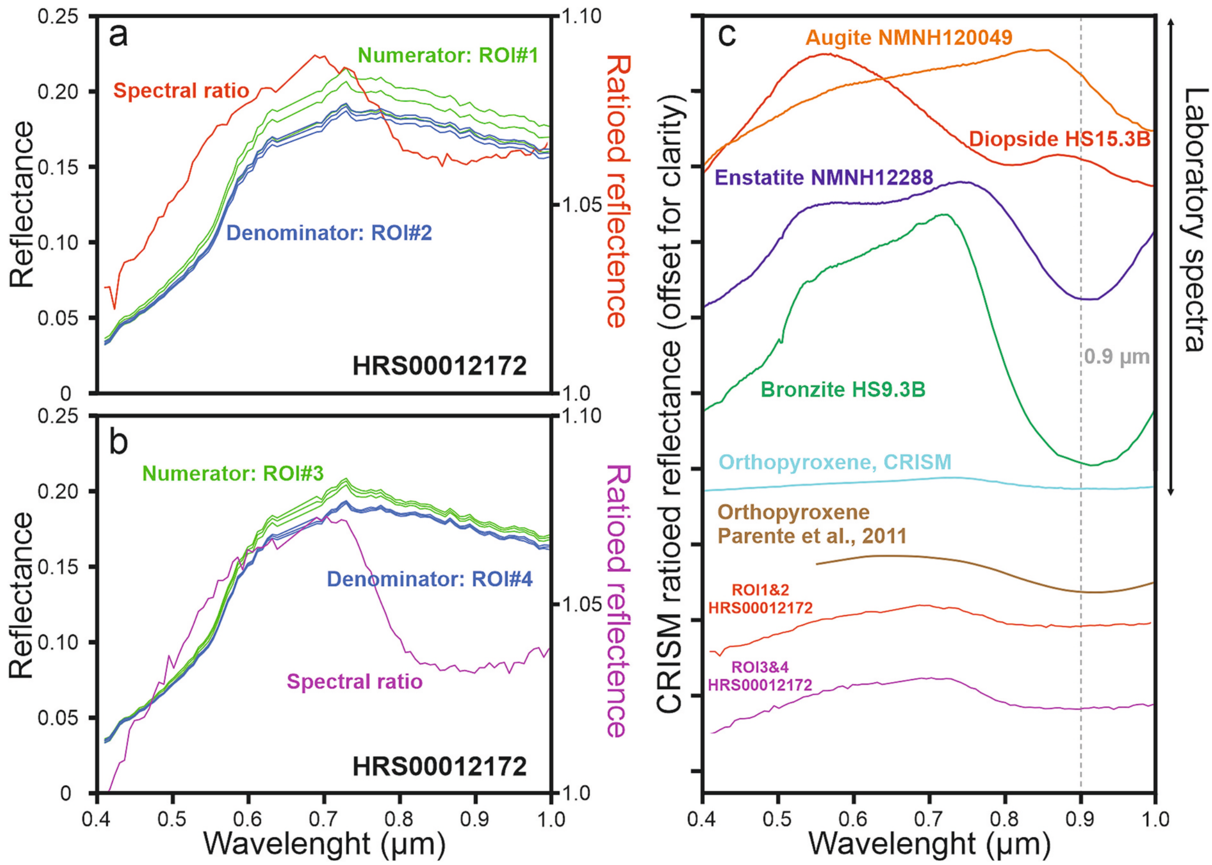

Fig. 10. Plots showing spectral characteristics in the visible and near-infrared range (0.4–1.0 µm) of the studied mounds (Fig. 8) and their comparative analysis to the reference laboratory-derived spectra of pyroxenes and Martian LCP-rich outcrop. **(a-b)** Spectral data of nominators (green), denominators (blue) (ROI#1 = 66 px; ROI#2 = 15 px; ROI#3 = 24 px; ROI#4 = 12 px) and their ratioed spectra from locations indicated by the corresponding arrows in (Fig. 8b). Please note that we included the min, max and mean spectrum for the regions of interest to show the consistency of the spectral signature throughout these regions. **(c)** The comparison of the laboratory-derived spectra of pyroxenes including augite, diopside, enstatite, and bronzite from the USGS spectral library (Clark et al., 2007) as well as orthopyroxene (CASB51) derived from the CRISM spectral library (https://speclib.rsl.wustl.edu/search.aspx; available at 30.01.2023). In addition, we redrew a LCP spectra obtained by Parente et al. (2011) for LCP-rich mound. The grey dashed line marks the location of the absorption at 0.9 µm after Viviano-Beck et al. (2014) which is considered diagnostic for LCP. The divisions of the vertical axis are 0.1. (For interpretation of the references to colour in this figure legend, the reader is referred to the web version of this article.)

terrestrial scoria cones or tuff rings/cones and their putative Martian analogues (Brož and Hauber, 2012, 2013; Brož et al., 2017). In addition, the mapped mounds do not generally show well-developed central summit craters that would constitute signs of explosive-dominated activity, but they reveal the presence of putative volcanic fissures (Figs. 2g-j and 6). On Earth, similar morphologies of elongated edifices with central ridges or fissures are common for lava cones (e.g., Hekla volcanic system; Gudmundsson et al., 1992; Höskuldsson et al., 2007; or the Caviahue-Copahue complex in the Andes; Melnick et al., 2006). In such case, central ridges resemble manifestations of subsurface dikes (Fig. 14a–b; Gudmundsson et al., 1992; Pedersen et al., 2020) and central fissures are often associated with terrestrial dike-fed volcanoes (Acocella and Neri, 2009). However, one of the best-preserved examples of the edifices are CF02–03 which show similar morphology to the Laki-type edifices in Iceland (Fig. 14c–f). On Earth, such edifices are formed as the result of lava spattering after low energetic explosive eruptions without the involvement of water/ice leading to the formation of spatter cones and scoria cones (Reynolds et al., 2016). Although these edifices show similarities to terrestrial explosive volcanoes, the similarly sized Martian putative scoria cones described from the Ulysses Fossae region (Brož and Hauber, 2012), and Hydraotes Chaos (Meresse et al., 2008; Brož et al., 2015), or the putative Martian phreatomagmatic edifices (Brož and Hauber, 2013) resulting from low energetic explosive-dominated eruptions do not share similar morphologies and slope characteristics. They mainly form circular (in plan view) edifices with summit craters and are characterized by smooth slopes compared to more irregular to elongated edifices with steep and blocky-textured slopes from the Claritas Fossae region. Altogether, the evidence favors a predominant role of effusive eruptions, however, localized explosive episodes cannot be fully discarded.

We also compared the morphology of the studied mounds with terrestrial subglacial volcanic edifices. At first glance, the studied edifices indeed share some similarities, i.g., common elongations and alignments, steep slopes, the blocky texture of flanks, lack of summit craters, with subglacial volcanic edifices, for example with elongated edifices called tindars that are formed by effusive eruptions under the ice (Pedersen et al., 2020). In such case, the eruptive style is controlled by pressure and the presence of ice/water. However, the studied edifices also do not show signs of phreatomagmatic activity which might be present if lava would have been in contact with ice/water (e.g., Brož and Hauber, 2013). Moreover, we did not observe evidence indicating extensive glacial processes within the studied area. Thus, we consider the subglacial origin of the studied edifices as unlikely due to the regional geological context.

Although most of the studied mounds are not associated with flow-like units, in one case we found a central conical-shaped mound (CF25; Fig. 1c) surrounded by a caldera-like rim or collapse scar (Figs. 4 and 7), and short flow-like features (Figs. 5a and 6c–d) characterized by

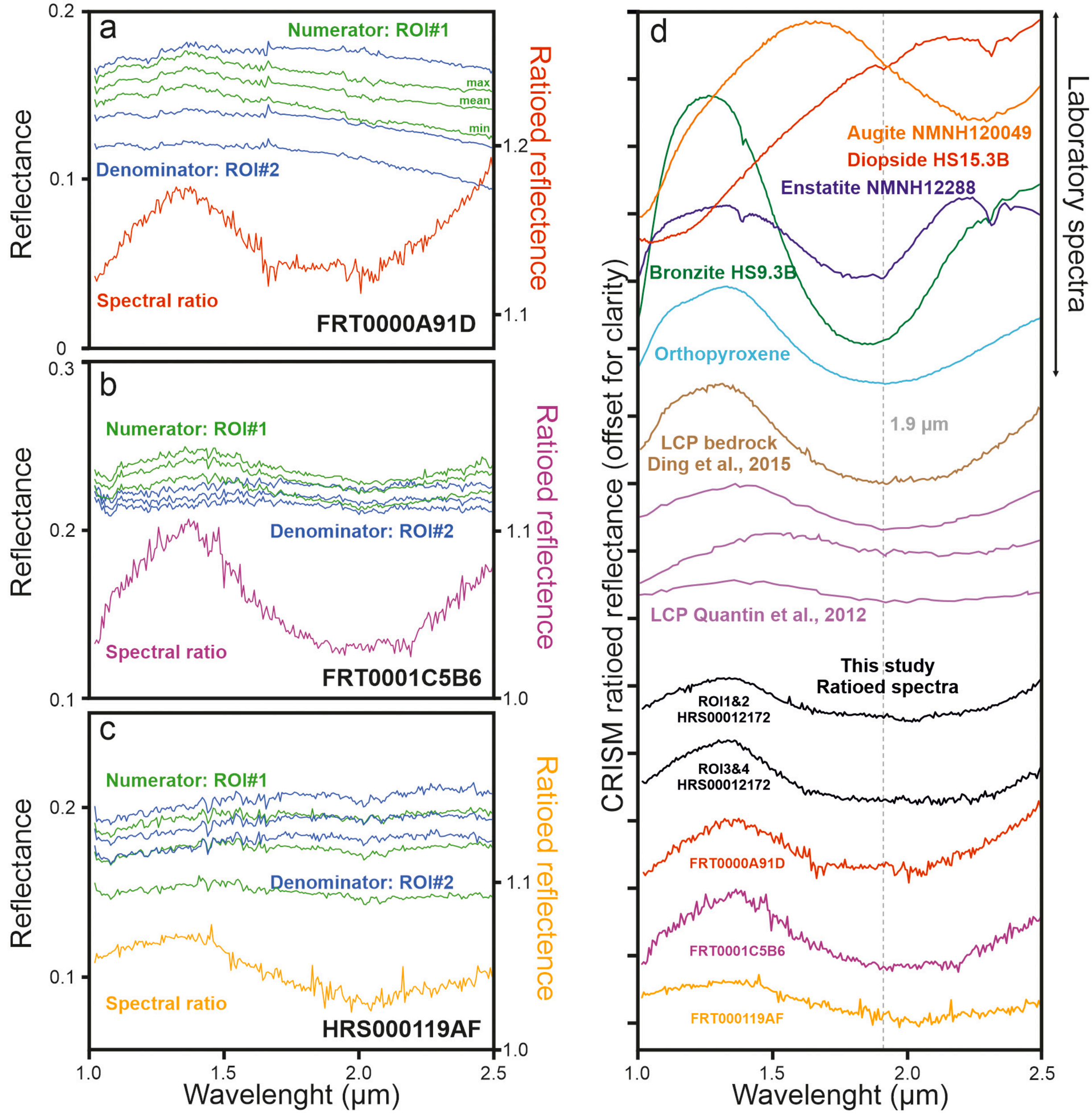

Fig. 11. Plots showing spectral characteristics of the studied mounds (Fig. 9) and their comparative analysis to the reference laboratory-derived spectra of pyroxenes, Martian LCP-rich outcrops, and ratioed spectra from Fig. 8. **(a-c)** Spectral data of nominators (green), denominators (blue) (FRT0000A91D, ROI#1 = 51 px and ROI#2 = 45 px; FRT0001C5B6, ROI#1 = 20 px and ROI#2 = 11 px; HRS000119AF, ROI#1 = 15 px and ROI#2 = 15 px) and their ratioed spectra from locations indicated by the corresponding arrows in (Fig. 9b-d). Please note that we included the min, max and mean spectrum for the regions of interest to show the consistency of the spectral signature throughout these regions. **(d)** The comparison of the laboratory-derived spectra of pyroxenes including augite, diopside, enstatite, and bronzite from the USGS spectral library (Clark et al., 2007) as well as orthopyroxene (CASB51) derived from the CRISM spectral library (https://speclib.rsl.wustl.edu/search.aspx; available at 06.07.2023). In addition, we redrew the selected LCP spectra obtained by Quantin et al. (2012) for impact craters in the Thaumasia region and Ding et al. (2015) for LCP-rich bedrock. The grey dashed line mark the location of the absorption at 1.9 μm after Viviano-Beck et al. (2014), which is considered diagnostic for LCP. The divisions of the vertical axis are 0.1. (For interpretation of the references to colour in this figure legend, the reader is referred to the web version of this article.)

irregular lobate shape boundaries. They are similar in appearance to flows associated with putative scoria cones in Ulysses Fossae (Brož and Hauber, 2012), Hydraotes Chaos (Meresse et al., 2008; Brož et al., 2015), and Coprates Chasma (Okubo, 2016; Brož et al., 2017). In these regions, such flow units have been interpreted as lava flows (Brož and Hauber, 2012; Brož et al., 2017). Moreover, in the southern part of the central cone of CF25, HiRISE imagery reveals the presence of putative volcanic fissure-originating deposits that cover the older highlands (Fig. 6d).

We therefore propose the following scenario that leads to the formation of this edifice associated with lava flows (CF25). Firstly, the former edifice was built by low-volumetric volcanic activity during which effusive and explosive activity occurred. This led to the formation of lava flows as well as the production of scoria material which gave a rise to a volcanic edifice (Fig. 5b; stage 1). Further development included the collapse of the central part of the former edifice and/or the partial destruction of the summit area of the edifice due to an explosive eruption (Fig. 5b; stage 2). We consider the second scenario as less

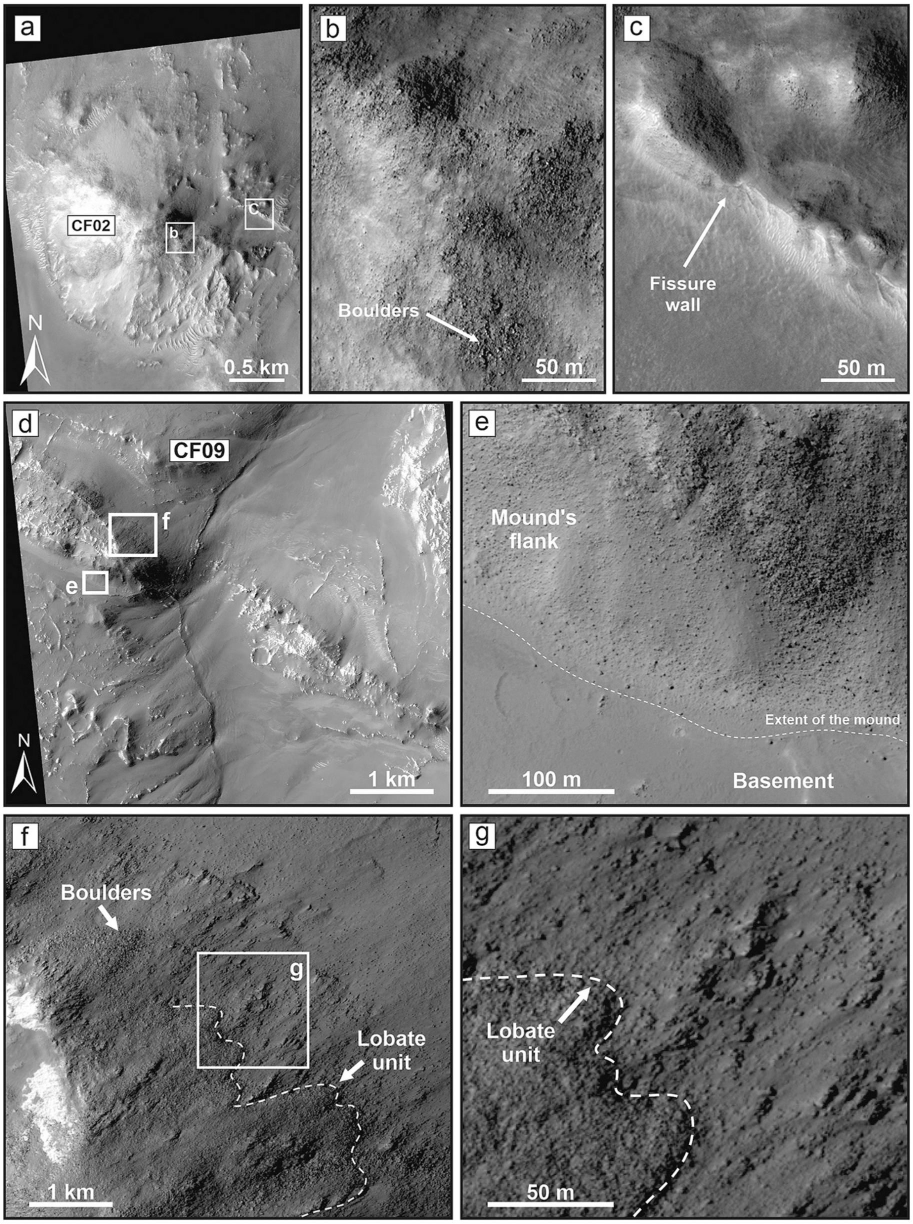

Fig. 12. An overview image **(a)** of the CF02 mound with central fissure (HiRISE image ESP_012771_1520, centered at 27.629°S, 252.848°E). **(b)** The close-up image reveals that the mound flanks are covered by meter-sized boulders. **(c)** Image showing the northern wall of the central putative volcanic fissure indicating the limited slope erosional processes. In addition, to the north of the fissure, the mound's flank is covered by boulders. **(d)** An overview image of the CF09 elongated mound (HiRISE image ESP_077031_1515, centered at 28.294°S, 254.558°E). **(e)** The southern part of the mound with a well-visible boundary between the flank covered by boulders and the smooth-appearing basement. **(f)** The northern flank of the studied mound with flow-like units with lobate margins (marked by white dashed line) that originate from the central fissure. **(g)** Close-up image showing the flow-like unit and the mound flanks' texture comprising blocks and boulders.

plausible due to the lack of large boulders, not found on the HiRISE image (ESP_76556_1510; Fig. 6) in the vicinity of the edifice. After the caldera-like rim formation, the volcanic activity likely continued forming the central edifice with steep flanks (Table 2) and short lava-flows (Figs. 4g and 7). As the outer flanks of the caldera-like rim (primary edifice) of the CF25 cone is characterized by a smoother surface, compared with the surrounding lowland terrains, we argue that it is likely composed of or covered by fine-grained deposits. In contrast, the HiRISE-based observations of the inner cone revealed that the slopes have blocky texture with meter-sized boulders (Fig. 6b). We suppose that the time spacing between the caldera formation and the rebuilding of the central edifice was relatively short, otherwise the magma source would have been plugged and the volcanic activity displaced. The structure and morphological parameters of the studied cone together with the associated short lava flows show similarities to terrestrial composite volcanoes (Karátson et al., 2010; Cas et al., 2022) suggesting the co-occurrence of effusive and explosive eruptions. A volcanic origin of this edifice is also supported by similar-sized terrestrial analogues (Fig. 5c–d) of post-caldera volcanoes such as Anak Krakatau volcano island (~2 km in size) situated within the submarine caldera (~7 km in diameter) formed after the Krakatau eruption in 1883 in Indonesia (Dahren et al., 2012 and references therein), Las Cañadas caldera (~16 km in length), on the island of Tenerife (Canary Islands), which hosts the active volcanic complex Teide-Pico Viejo (Martí, 2019), Vesuvio volcano (~3 km in size) in Italy (Tadini et al., 2017), and the rebuilding of the Bezymianny volcano (~2 km in size) with associated lava flow unit in Kamczatka (Shevchenko et al., 2020).

Another evidence on the origin of the studied edifices might be provided by mineralogical constraints. Based on previous analyses of CRISM spectral signatures, the Claritas Fossae region is considered to host typical mafic minerals such as olivine and pyroxene of magmatic origin as well as hydrated sulfates and phyllosilicates (Dohm et al., 2009 and references therein). These studies reported LCP-rich rocks locally outcropping within the eastern highlands of Claritas Fossae often associated with olivine-rich material. Here, we note that the studied edifices are spatially associated with LCP-rich rocks/materials suggesting an igneous origin, and that the surrounding terrains reveal distinctly different mineralogical characteristics. The most significant

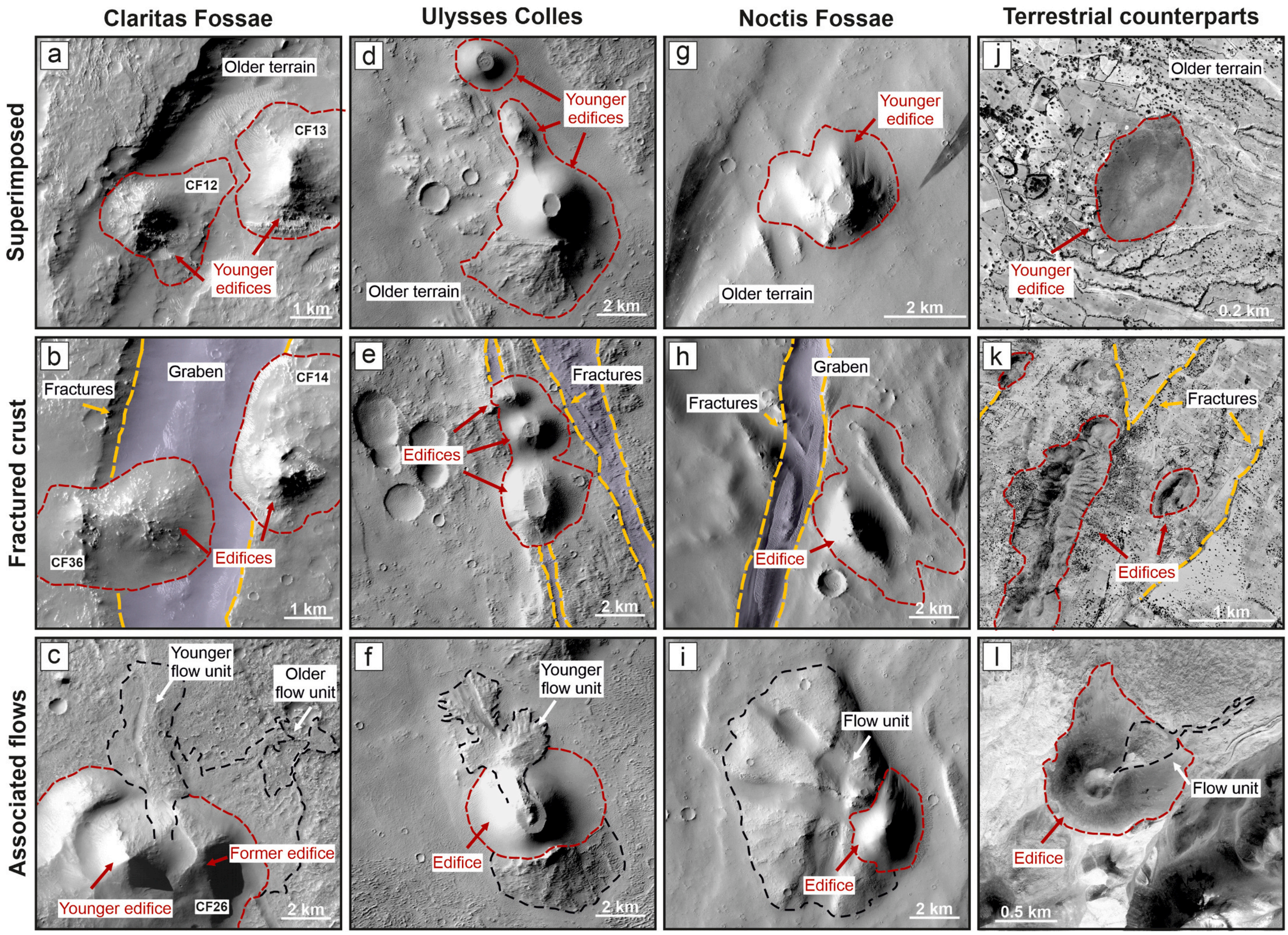

Fig. 13. A comparison of investigated edifices with selected Martian and terrestrial counterparts. All edifices are classified into three groups (horizontal rows) based on common morphological features including association with 1) flow units, 2) fractured terrain as the basement, and 3) superposition of the edifices on the older terrain. The edifices within the clusters of the Ulysses Colles and Noctis Fossae region have been previously described by Brož and Hauber (2012) and Pieterek et al. (2022a, 2022b) as Martian equivalents to terrestrial scoria cones. The CTX images details: **(a-c)** Claritas Fossae (P18_008156_1516, centered at 28.54°S, 254.62°E; B20_017439_1503, centered at 29.84°S; 253.2°E; P13_005954_1529, centered at 27.17°S, 259.9°E); **(d-f)** Ulysses Colles (P19_008262_1862, centered at 6.27°N, 236.97°E); **(g-i)** Noctis Fossae (F04_037508_1798, centered at 0.26°S, 261.15°E; G15_024269_1780, centered at 2.03°S, 260.96°E; F02_036664_1787, centered at 1.38°S, 263.74°E); **(j-l)** terrestrial counterparts including elongated edifices from Afar triangle in Ethiopia (7°52′24.57″N, 38°54′55.07″E and 7°48′15.99″N, 38°52′17.43″E) and volcanic cone with flow unit located on Hawai'i island (19°51′12.19″N, 155°26′4.30″W). All images are north-oriented.

concentrations of LCP mainly occur within the central fissure and on the edifice flanks (Figs. 8–9) indicating that igneous material likely originated from the studied edifices due to volcanic eruptions.

Finally, it has to be noted that our mapping suggests that the studied field might host more landforms that might have been formed by the same processes as the mapped mounds, however, their shapes and sizes (Fig. 4f) do not allow us a clear distinction so they have been excluded from our analysis. We also cannot exclude the possibility that the population of these mounds was formerly more numerous, but due to the later volcanic activity some of the mounds were buried by younger lava flows covering wide areas in the western edge of the study area (see Fig. 1c for details).

5.2. Age and tectonic constraints

The formation of the Claritas Fossae is interpreted to result from a mantle plume-driven activity accompanied by tectonic, volcanic, and hydrothermal activity (Dohm et al., 2009). Based on the high density of impact craters, complex structure, and a possible magnetic signature, Dohm et al. (2009) noted that the formation of the Claritas rise occurred during an ancient period of Mars' evolution and likely predates the development of Tharsis or marks its incipient development. Evidence of the first volcanic activity after the formation of the Claritas region is the existence of large-scale volcanic massifs (Fig. 1) dispersed throughout the Thaumasia region (Dohm and Tanaka, 1999; Grott et al., 2005, 2007; Hauber and Kronberg, 2005). Grott et al. (2005) investigated one of the large extensional structures in the Coracis Fossae interpreted as rifts (Dohm and Tanaka, 1999; Dohm et al., 2001). At one of these rifts, a large-scale volcanic massif is cut by rift-related fractures and must therefore be older or formed at the early stages of rifting (Grott et al., 2005). Based on the aforementioned structural cross-cutting relationships combined with the age determination of rift-related structures, Grott et al. (2005) attributed a maximum age of rifting and set the lower age limit of large-scale volcanic massifs at ~3.9 Ga.

In addition to Coracis Fossae, a similar large-scale volcanic massif is located within the Claritas Fossae highland region (Dohm and Tanaka, 1999) being cut by N-S-trending fractures. Based on fault-buffered crater counting, Vaz et al. (2014) and Smith et al. (2009) determined the most probable time interval of faulting in Claritas Fossae between 3.4 and 2.5 Ga (Table 3). This age supports the conclusion that these volcanic massifs had been formed before the Late Hesperian - Early Amazonian tectonic activity within the Thaumasia highland belt, including Coracis

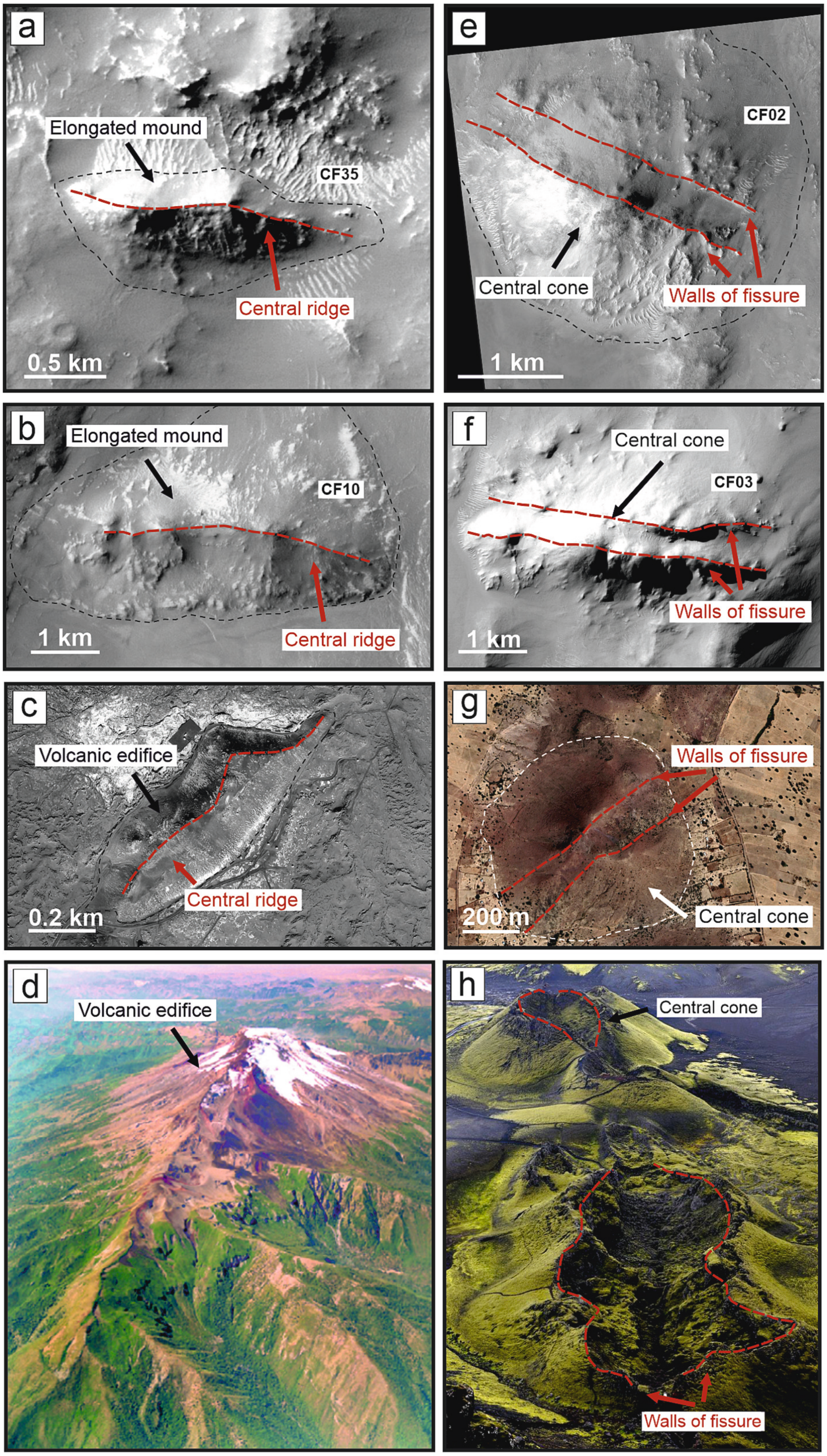

Fig. 14. A comparison of investigated mounds with selected terrestrial volcanic constructs. **(a-b)** The elongated mounds with a central ridge at the summit (CTX image P18_007945_1532, centered at 26.89°S, 255.27°E and CTX image D15_033091_1519, centered at 28.18°S, 254.83°E). **(c)** Terrestrial volcanic landform that is characterized by a summit ridge that manifests the presence of the subsurface dike (63°50′11.70″N, 22°39′30.91″W). **(d)** Oblique aerial photo to the northeast showing the Callaqui volcano in the Andes (Chile). The photo is adapted after Melnick et al. (2006). **(e)** The circular mound (CF02) that shows a central fissure and blocky texture of its flanks (HiRISE image ESP_012771_1520, centered at 27.63°S, 252.85°E). **(f)** Elongated mound (CF03) with well-distinguishable central fissure characterized by steep-appearing walls and blocky flanks (CTX image B20_017439_1503, centered at 29.84°S, 253.2°E). All images are north-oriented. **(g)** The conical-shaped volcano edifice dissected by the volcanic fissure at East Ziway volcanic field in the Main Ethiopian Rift (7°50′15.32″N, 38°53′32.67″W) **(h)** The image of the Laki elongated volcanic edifices showing a central fissure with steep walls (64°4′1.82"N, 18°14′50.39″W). Credit: Ian Strachan (pinterest.com; available on 10.11.2022).

and Claritas Fossae. As all studied small-scale edifices and their associated deposits studied here, are superimposed on N-S-trending fractures, they therefore represent a younger episode of volcanic activity compared with the large-scale volcanic massifs of the Thaumasia region.

To reveal the lower age limit of the Claritas' edifices formation, we considered the spatial relationship of the WNW-ESE aligned and elongated edifices CF09 and CF11–12 (Fig. 1c) and the N-S-trending fault bounding the Thaumasia graben and eastern highlands of Claritas Fossae. These edifices are situated on both sides of the bounding fault and display a difference of >2000 m in the elevation of their basements. The edifices being emplaced by a common volcanic event and by the same supplying dike(s) must have predated the subsidence of Thaumasia

Table 3
The comparison of two different age scenarios considered in this study together with their implications. These data refer to Sections 5.1–5.3.

Age scenario	Single episode	Two episodes
Age	from 3.4 to 2.5 Ga Hesperian to Early Amazonian	main activity in the Hesperian to Early Amazonian and a younger volcanic episode in the Middle/ Late Amazonian (< ~2.0 Ga)
Evidence of superposition	● Predating the formation of Thaumasia graben (Late Hesperian/Early Amazonian; Tanaka and Davis, 1988; Hauber and Kronberg, 2005) and postdating the N-S faulting of Claritas Fossae (assigned from 2.5 to 3.4 Ga; Smith et al., 2009; Vaz et al., 2014)	Not observed
Morphological evidence	● Structural relationship with the WNW-ESE-trending Noachian-age ridges (Fig. 1). ● Occurrence of the edifices on both sides of fault zone bounding Thaumasia graben and highlands of Claritas Fossae (Fig. 1). ● Association of edifices and LCP-dominated deposits that indicate Noachian/Hesperian-age magma composition (Figs. 8–9).	● Higher absolute heights and slope angles compared to other Amazonian-age small-scaled volcanoes on Mars (Fig. 4). ● Blocky structure of the edifices, associated with meter-scale boulders on flanks (Figs. 6 and 10). ● Presence of the putative volcanic central fissures that are not significantly infilled by sediments revealing an almost pristine fissure walls (Fig. 12).
Implications	● Confirms that old highly crater and faulted terrains that escaped the lava plains resurfacing constitute an insight into old volcanism. ● Support the hypothesis that Noachian/Hesperian terrains are associated with LCP-dominated volcanism. ● Magma was transported by the old and reactivated WNW-trending pathways.	● Presence of LCP-dominated volcanism indicate high degree of partial melting due to a warmer mantle (upwelling zone) beneath Claritas Fossae. ● Accordance with the thermal modelling of the Martian mantle by Plesa et al. (2018, 2023). ● Presence of local-scale magma heterogeneities that indicates different and more varied crystallization pathways than Amazonian-age basaltic lavas (Viviano et al., 2019).

graben. In the opposite scenario, if the edifices would have been emplaced after the formation of the eastern bounding fault of the Thaumasia graben, we might expect that the difference in elevation between the Thaumasia graben and Claritas Fossae highlands would have prevented the formation of the edifices in the eastern highlands or in the western Thaumasia graben. Hence, the volcanic activity must have ended before the main stage of Thaumasia tectonics, which has been constrained to occur in Late Hesperian or Early Amazonian (Tanaka and Davis, 1988; Hauber and Kronberg, 2005) (Table 3).

Such relatively old ages might be challenged by the “fresh-looking” appearance of the studied edifices (Table 3). The comparative analysis of morphological parameters demonstrated that the studied edifices show higher absolute heights and slope angles compared to other Amazonian-aged small-scaled putative volcanoes on Mars (Fig. 4). Assuming a Hesperian age of the edifices, we would expect to identify more intensely eroded edifices compared with Amazonian-aged edifices found in Ulysses Colles (Brož and Hauber, 2012), Coprates Chasma (Brož et al., 2017), and Noctis Fossae (Pieterek et al., 2022b) (Fig. 13). Moreover, for some of the mapped edifices, we identified putative volcanic central fissures that are not significantly infilled by sediments revealing the almost pristine fissure walls (Figs. 12 and 14). This indicates the limited effect of the erosional processes. Considering even smaller-scale observations using HiRISE images, we found a significant number of boulders associated with the studied edifices that are well-preserved on their slopes (Fig. 12). This observation also challenges the Hesperian age of the volcanic edifices as these boulders should be disintegrated since ~3 billion years after the latest volcanic eruption might have occurred (De Haas et al., 2013). We argue that the good state of preservation of the studied edifices is similar to that of the northern Noctis Fossae cones that are interpreted to be the youngest among the Noctis Fossae volcanic field and were attributed to Late Amazonian volcanic activity (Pieterek et al., 2022b). These considerations indicate that within the Claritas Fossae region, we might consider two different scenarios with respect to the ages of the studied edifices. In the first scenario, the entire studied Claritas Fossae volcanic field might have been formed by a single episode of volcanic activity occurring within a relatively limited period of time (e.g., Late Hesperian or Early Amazonian). Such interpretation is supported by the spatial distribution of the studied edifices as they are aligned and elongated in a common WNW direction. Moreover, our mineralogical analysis showed that a LCP-rich composition has been determined for edifices characterized by different states of preservation emplaced throughout the studied region. Assuming different volcanic episodes of various ages, we might expect different magma compositions. However, in the second scenario, which is partially opposed to the first one, we can assert that the majority of the edifices have been emplaced according to the first scenario, whereas only the best-preserved edifices (e.g., CF25) might have been formed later, for example in Middle or Late Amazonian, exploiting older fault sets as pathways for magma ascent. Such a scenario with at least two episodes of volcanism, one of them being relatively young, might explain the pristine morphology of some edifices and be consistent with very recent high melt fractions beneath Claritas Fossae (Plesa et al., 2023). Moreover, this scenario may also imply that high melt fractions could have been formed throughout the entire Amazonian period as edifices of different states of preservation reveal LCP-rich surfaces. However, in order to confirm any of the above presented scenarios with certainty, further investigations on the tectonic evolution of the Thaumasia region are needed, especially in terms of its chronology.

Considering the spatial distribution of the studied edifices, our mapping demonstrates that they occur only at the highly fractured terrains and are aligned in a WNW direction. This alignment is further supported by their individual elongations showing an average value of N111E (Table 2). These orientations are in accordance with WNW-ESE-trending topographic highs of rugged Noachian terrain (Fig. 1b) mentioned by Hauber and Kronberg (2005), which are almost perpendicular to the majority of the fractures. In addition, the spatial distribution of the large-scale volcanoes mapped in the Thaumasia region by Dohm and Tanaka (1999) and Dohm et al. (2001) indicate their alignment in a NW-SE-trending orientation. Hence, the formation of the studied edifices might have been controlled by inherited faults once responsible of the WNW-ESE-trending topographic highs (Hauber and Kronberg, 2005) and reactivated simultaneously and/or after the Thaumasia graben and Claritas Fossae faulting (~3.4 Ga; Vaz et al., 2014). However, if the age of some of the studied edifices would turn out to be much younger (e.g., Middle/Late Amazonian), their formation could have been supported by the presence of high fractions of very recent partial melts that might still occur beneath Claritas Fossae or its close vicinity (Plesa et al., 2023), and which may have used the fractured crust for their ascent.

5.3. *Magma composition through time*

Using CRISM spectral data, we note that the studied edifices are associated with LCP-dominated material mainly occurring within central fissures and flanks (Figs. 8–9). On Mars, LCPs are most abundant in Noachian-aged terrains, suggesting that aluminum and calcium were likely incompatible with the early mantle-derived igneous melts (Mustard et al., 2005). Such LCP-dominated mineralogy of volcanic edifices contrasts to typical basaltic compositions that are common on Mars (Christensen et al., 2000; McSween Jr., 2015; Viviano et al., 2019). It is through that pyroxene composition change as a function of geological time on Mars, being the transition between LCP and HCP proposed close to the Noachian/Hesperian boundary (Mustard et al., 2005; Poulet et al., 2009; Flahaut et al., 2011; Baratoux et al., 2013; Grott et al., 2013). Poulet et al. (2009) inferred that the formation of LCP in the Noachian times might be associated with higher degrees of partial melting or the crystallization of water-rich magma. In contrast, Baratoux et al. (2013) highlighted that this transition might be caused only by the thermal evolution of the Martian mantle.

Based on the investigations of the mineralogy of impact craters, Quantin et al. (2012) reported the presence of massive rocks dominated by LCP within the impact craters in the Coracis Fossae region and inferred that they represent primitive pre-Noachian Martian crust. Moreover, Skok et al. (2012) investigated the unaltered mafic (dunitic and pyroxenitic in compositions) central peaks of large impact craters and suggested that the earliest formed magmas in the ancient Martian crust were formed by fractional crystallization within large near-surface magma reservoirs forming cumulates. Such interpretation of LCP crystallization might be also supported by the only orthopyroxenite cumulate (ALH 81004) among Martian meteorites which were probably formed by fractional crystallization of basaltic parental melts (Mittlefehldt, 1994) showing a formation age of ~4.1 Ga (Lapen et al., 2010). The age of the orthopyroxenite cumulate indicates magmatism on Mars started in the Early Noachian (Lapen et al., 2010) and continued, for example, within Tharsis until the Late Amazonian (Neukum et al., 2004; Krishnan and Kumar, 2022; Pieterek et al., 2022a). On the other hand, Martian shergottites whose source is thought to be mainly the Tharsis region (Fritz et al., 2005; Lagain et al., 2021) show varied mineralogical contents comprising from ~30% up to ~45% of LCP (orthopyroxenes) (Papike et al., 2009). Based on the CRISM-derived compositional distribution within the Tharsis region, Viviano et al. (2019) suggested that although global evolution of volcanic composition had occurred at the end of Noachian, the local-scale magma heterogeneities with respect to composition might have persisted through the Amazonian recording different and more varied crystallization pathways than young basaltic lavas.

However, to provide more in-depth insights, geological reconstruction including volcanic and tectonic processes of Claritas Fossae seems to be crucial. Therefore, considering the formation time of the LCP-rich edifices investigated in this study, we conclude that they might represent evidence of Hesperian or, alternatively, even younger Amazonian volcanism (Table 3) sourced by LCP-dominated melts (Fig. 8d). Under the Hesperian "old formation" scenario, the ascending melts possibly related to the high degree melting might have been stored in near-surface magma reservoirs and erupted as volatile-poor pyroxene-rich magma forming steep slope edifices. However, if some of the studied edifices are younger and they have been formed in the Middle to Late Amazonian, our study might have implications for understanding the evolution of the Martian mantle and local Tharsis magmatic plumbing systems. The LCP-rich melts can be produced by high degrees of partial melting due to a warmer mantle (upwelling zones) and/or melting at lower pressure below a thin lithosphere (Brustel, 2021). The second scenario is less likely due to the inferred thickened crust below the Tharsis rise that reaches >50 km (Bouley et al., 2020). Constraints on partial melting can be derived by thermal modelling of the Martian mantle conducted by Plesa et al. (2018, 2023). Assuming two different crustal scenarios, Plesa et al. (2023) inferred a higher present-day heat flux and high melt fraction zones that are most likely emplaced beneath Tharsis and Elysium provinces. In the first scenario that assumes a pronounced crustal thickness dichotomy with homogenous crustal density, the highest melt fractions occur directly beneath the Claritas Fossae and Syria Planum regions (Plesa et al., 2023). The second scenario that is characterized by a difference in crustal density between the northern and southern hemispheres shows the highest melt fractions emplaced south of Tharsis Montes and beneath Noctis Fossae. Both scenarios suggest that partial melts may still be produced in the Martian interior today. Therefore, the occurrence of very recent high melt fraction zones either directly beneath Claritas Fossae or in its vicinity (Plesa et al., 2023) might support the potential Amazonian volcanic activity supplied by LCP-rich melts. This implies that LCP-rich volcanism might not have been only restricted to ancient times on Mars (Viviano et al., 2019).

Based on the large-scale Thaumasia volcanoes, which represent a record of the first volcanic activity in the Thaumasia region, Dohm and Tanaka (1999) demonstrated that these volcanic massifs have been formed throughout most of the Noachian and into the Early Hesperian periods displaying evidence of explosive volcanism. The explosive eruptions might result from volatile-rich magma or the interaction of magma and subsurface water or ice deposits (Dohm and Tanaka, 1999). In contrast, the Claritas' edifices, except for one example (Fig. 5), indicate the significant contribution of low-volume effusive eruptions forming steep-appearing edifices without associated lava flows (Fig. 3). Some of these edifices might represent remnants of the original supplying dikes exposed on the surface. In addition, the studied edifices are associated with LCP-rich surfaces that might indicate an important role of mantle-derived partial melts. Interestingly, the CF25 edifice in the easternmost part of the Claritas Fossae which likely experienced effusive and explosive eruptions suggests a more complex evolutional volcanic history of the studied volcanic field. In that case, a change in the eruptive style might be related to a higher amount of gases at the final stages of eruption. Altogether our observations suggest that the studied volcanic field was mainly shaped by effusive volcanism with probably limited episodes of explosive eruptions leading to the formation of a composite edifice (Fig. 5). A compilation of previous results related to the ancient large-scale volcanoes that were likely formed >3.9 Ga (Grott et al., 2005) together with our findings indicates that the first volcanic activity in Thaumasia was controlled by large-volume explosive-dominated eruptions, whereas younger small-scale volcanoes, studied here, were made by effusive eruptions of LCP-rich viscous and volatile poor magmas. However, two plausible scenarios of the chronology of volcanic episodes can still be considered 1) a single episode of Hesperian-Early Amazonian volcanism inferred from the structural relationship with the tectonic features, and 2) two volcanic episodes, one in the Hesperian to Early Amazonian, and a later one in the Middle to Late Amazonian, as inferred from the fresh morphological appearance of some individual edifices and the comparative analysis to other Martian volcanic fields (Table 3). Thus, our study of the volcanic evolution of the Thaumasia region suggests that the majority of the studied edifices are linked to the late-stage migration of LCP-rich magmas in dikes exploiting reactivated WNW-ESE tectonic pathways, whereas probable younger volcanic events likely used pre-existing fractures related to the complex tectonic evolution of the Thaumasia graben and Claritas Fossae region. The two-episode scenario of the volcanism in Claritas Fossae might have resulted in the formation of well-preserved edifices (e.g., CF25) of Amazonian age whose occurrence might be supported by the most recent modelling of the spatial distribution of very recent high melt fractions underneath the Martian lithosphere (Plesa et al., 2023). High partial melting zones emplaced, in one of the crustal scenarios, beneath Claritas Fossae may provide an explanation for the potential sources of LCP-rich magmas. However, to fully understand the spatiotemporal evolution of this complex volcanic field, further investigations on the tectonic evolution of the Thaumasia region are needed in order to provide detailed chronological constraints for the volcanic reconstructions.

6. Conclusions

We propose that the studied edifices in the Claritas Fossae region were formed due to volcanic activity sourced by low-volumetric volcanic eruptions fed by subsurface dike(s). The spatial distribution and elongations of the studied edifices indicate WNW-ESE tectonic structures controlling the emplacement of the dike(s), which are discordant with the predominant N-S faults of the region. The observed orientations might suggest that feeder dikes inherited the orientation of pre-existing fractures related to old NW-SE-trending ridges of Noachian-aged crust or NW-aligned large-scale volcanoes situated within the Thaumasia region. The detailed investigation of the edifice morphology leads us to conclude that the volcanic field experienced mainly effusive eruptions of viscous, volatile poor magmas. However, we also noted the presence of one of the best-preserved kilometer-sized composite volcanoes associated with a caldera-like rim on Mars whose formation was likely controlled by both effusive and explosive eruption styles. The superposition relationships between the edifices and fractured terrain allow us to conclude that the most of the edifices within the volcanic field might have been formed between the Late Hesperian and the Early Amazonian. However, for some of the edifices, there is morphological evidence such as well-preserved volcanic fissures and fresh-appearing slopes that challenge these structural-based considerations. Therefore, we also propose an alternative scenario assuming a second, Middle/Late Amazonian episode of the volcanism in the Claritas Fossae region.

The obvious spatial association between the volcanic edifices and LCP-rich surface compositions suggests eruptions of relatively primitive magma likely produced by a high degree of partial melting. The LCP-rich composition of the studied edifices might support the older, Hesperian-age scenario confirming the hypothesis that LCP-dominated volcanism is spatially related to ancient terrains. However, on the other hand, assuming a Middle to Late Amazonian age for some of the edifices, the studied volcanic field might bear evidence of the occurrence of local magmatic systems generating LCP-rich melts in the Amazonian period, with implications for the petrological and geochemical evolution of Mars. Altogether, the morphological and spectral characteristics of the small-scale edifices in the Claritas Fossae region appear to be quite different in relation to other volcanic fields of similar geological settings observed so far on Mars. This underlines the importance of studying old and heavily fractured terrains on Mars that escaped the later resurfacing caused by widespread and younger lava flows. Therefore, such investigations might provide previously unexplored knowledge about the evolution of the Martian magmatic systems.

Declaration of Competing Interest

The authors declare that they have no known competing financial interests or personal relationships that could have appeared to influence the work reported in this paper.

Data availability

Data are attached to this article in the Supplementary material.

Acknowledgements

This research was financially supported by the project “GEO-INTER-APLIKACJE” – high quality doctoral studies program conducted at the Faculty of Geographical and Geological Sciences of the Adam Mickiewicz University in Poznań no. POWR.03.02.00-00-I027/17 funded by the European Social Fund under the Operational Program Knowledge Education Development. We thank editor E. Rampe and two anonymous reviewers for their thorough and insightful comments that improved the manuscript. We thank Max Collinet for helpful discussions on Martian igneous petrology. BP would acknowledge A. Muszyński, W. Szczuciński, and K. Stattegger from the Adam Mickiewicz University in Poznań for reading the manuscript and engaging in discussion. B. Pieterek is financially supported by the Adam Mickiewicz University Foundation in the academic year 2022/2023. Elevation data have been processed using the MarsSI (marssi.univ-lyon1.fr) application founded by the European Union’s Seventh Framework Program (FP7/2007-2013) (ERC Grant Agreement No. 280168).

Appendix A. Supplementary data

Supplementary data to this article can be found online at https://doi.org/10.1016/j.icarus.2023.115770.

References

Acocella, V., Neri, M., 2009. Dike propagation in volcanic edifices: overview and possible developments. Tectonophysics 471, 67–77. https://doi.org/10.1016/j.tecto.2008.10.002.

Anderson, R.C., Dohm, J.M., Golombek, M.P., Haldemann, A.F.C., Franklin, B.J., Tanaka, K.L., Lias, J., Peer, B., 2001. Primary centers and secondary concentrations of tectonic activity through time in the western hemisphere of Mars. J. Geophys. Res. Planets 106, 20563–20585. https://doi.org/10.1029/2000JE001278.

Annen, C., Lénat, J.F., Provost, A., 2001. The long-term growth of volcanic edifices: numerical modelling of the role of dyke intrusion and lavaa-flow emplacement. J. Volcanol. Geotherm. Res. 105, 263–289. https://doi.org/10.1016/S0377-0273(00)00257-2.

Atwood-Stone, C., McEwen, A.S., 2013. Avalanche slope angles in low-gravity environments from active Martian sand dunes. Geophys. Res. Lett. 40, 2929–2934. https://doi.org/10.1002/grl.50586, 2013.

Balbi, E., Cianfarra, P., Ferretti, G., Crispini, L., Tosi, S., 2022. The Claritas Fossae region, an example of polyphasic deformation on Mars?, in: Europlanet Science Congress 2022. pp. EPSC2022-1041. https://doi.org/10.5194/epsc2022-1041.

Baptista, A.R., Mangold, N., Ansan, V., Baratoux, D., Lognonné, P., Alves, E.I., Williams, D.A., Bleacher, J.E., Masson, P., Neukum, G., 2008. A swarm of small shield volcanoes on Syria Planum, Mars. J. Geophys. Res. 113, 1–19. https://doi.org/10.1029/2007JE002945.

Baratoux, D., Pinet, P., Toplis, M.J., Mangold, N., Greeley, R., Baptista, A.R., 2009. Shape, rheology and emplacement times of small martian shield volcanoes. J. Volcanol. Geotherm. Res. 185, 47–68. https://doi.org/10.1016/j.jvolgeores.2009.05.003.

Baratoux, D., Toplis, M.J., Monnereau, M., Sautter, V., 2013. The Petrological Expression of Early Mars Volcanism, 118, pp. 59–64. https://doi.org/10.1029/2012JE004234.

Barsotti, S., Parks, M.M., Pfeffer, M.A., Óladóttir, B.A., Barnie, T., Titos, M.M., Jónsdóttir, K., Pedersen, G.B.M., Hjartardóttir, R., Stefansdóttir, G., Johannsson, T., Arason Gudmundsson, M.T., Oddsson, B., Þrastarson, R.H., Ófeigsson, B.G., Vogfjörd, K., Geirsson, H., Hjörvar, T., von Löwis, S., Petersen, G.N., Sigurðsson, E. M., 2023. The eruption in Fagradalsfjall (2021, Iceland): how the operational monitoring and the volcanic hazard assessment contributed to its safe access. Nat. Hazards. https://doi.org/10.1007/s11069-022-05798-7.

Bistacchi, N., Massironi, M., Baggio, P., 2004. Large-scale fault kinematic analysis in Noctis Labyrinthus (Mars). Planet. Space Sci. 52, 215–222. https://doi.org/10.1016/j.pss.2003.08.015.

Bleacher, J.E., Greeley, R., Williams, D.A., Cave, S.R., Neukum, G., 2007. Trends in effusive style at the Tharsis Montes, Mars, and implications for the development of the Tharsis province. J. Geophys. Res. Planets 112, 1–15. https://doi.org/10.1029/2006JE002873.

Bouley, S., Baratoux, D., Paulien, N., Missenard, Y., Saint-Bézar, B., 2018. The revised tectonic history of Tharsis. Earth Planet. Sci. Lett. 488, 126–133. https://doi.org/10.1016/j.epsl.2018.02.019.

Bouley, S., Keane, J.T., Baratoux, D., Langlais, B., Matsuyama, I., Costard, F., Hewins, R., Payré, V., Sautter, V., Séjourné, A., Vanderhaeghe, O., Zanda, B., 2020. A thick crustal block revealed by reconstructions of early Mars highlands. Nat. Geosci. 13, 105–109. https://doi.org/10.1038/s41561-019-0512-6.

Breuer, D., Moore, W.B., 2015. Dynamics and Thermal History of the Terrestrial Planets, the Moon, and Io. In: Schubert, G. (Ed.), Treatise on Geophysics. Elsevier, pp. 255–305. https://doi.org/10.1016/B978-0-444-53802-4.00173-1.

Brož, P., Hauber, E., 2011. Windows of old fractured crust and associated volcanism in Tharsis, Mars. In: European Planetary Science Congress. https://doi.org/10.1029/2011GL047310 p. EPSC-DPS2011-742-1.

Brož, P., Hauber, E., 2012. A unique volcanic field in Tharsis, Mars: pyroclastic cones as evidence for explosive eruptions. Icarus 218, 88–99. https://doi.org/10.1016/j.icarus.2011.11.030.

Brož, P., Hauber, E., 2013. Hydrovolcanic tuff rings and cones as indicators for phreatomagmatic explosive eruptions on Mars. J. Geophys. Res. Planets 118, 1656–1675. https://doi.org/10.1002/jgre.20120.

Brož, P., Bernhardt, H., Conway, S.J., Parekh, R., 2021. An overview of explosive volcanism on Mars. J. Volcanol. Geotherm. Res. 409, 107125. https://doi.org/10.1016/j.jvolgeores.2020.107125.

Brož, P., Čadek, O., Hauber, E., Rossi, A.P., 2015. Scoria cones on Mars: detailed investigation of morphometry based on high-resolution digital elevation models. J. Geophys. Res. Planets 120, 1512–1527. https://doi.org/10.1002/2015JE004873.

Brož, P., Hauber, E., Wray, J.J., Michael, G., 2017. Amazonian volcanism inside Valles Marineris on Mars. Earth Planet. Sci. Lett. 473, 122–130. https://doi.org/10.1016/j.epsl.2017.06.003.

Brož, P., Hauber, E., van de Burgt, I., Špillar, V., Michael, G., 2019. Subsurface sediment mobilization in the southern Chryse Planitia on Mars. J. Geophys. Res. Planets 124, 703–720. https://doi.org/10.1029/2018JE005868.

Brož, P., Oehler, D., Mazzini, A., Hauber, E., Komatsu, G., Etiope, G., Cuřín, V., 2023. An overview of sedimentary volcanism on Mars. EGUsphere 2023, 1–47. https://doi.org/10.5194/egusphere-2022-1458.
Brustel, C.P.A., 2021. Early Magmatic Processes on Mars. Vrije Universiteit Amsterdam.
Cas, R.A.F., Wolff, J.A., Martí, J., Olin, P.H., Edgar, C.J., Pittari, A., Simmons, J.M., 2022. Tenerife, a complex end member of basaltic oceanic island volcanoes, with explosive polygenetic phonolitic calderas, and phonolitic-basaltic stratovolcanoes. Earth-Sci. Rev. 230, 103990 https://doi.org/10.1016/j.earscirev.2022.103990.
Christensen, P.R., Bandfield, J.L., Smith, M.D., Hamilton, V.E., Clark, R.N., 2000. Identification of a basaltic component on the Martian surface from thermal emission spectrometer data. J. Geophys. Res. Planets 105, 9609–9621. https://doi.org/10.1029/1999JE001127.
Clark, R.N., Swayze, G.A., Wise, R.A., Livo, K.E., Hoefen, T.M., Kokaly, R.F., Sutley, S.J., 2007. USGS Digital Spectral Library splib06a, Data Series. Reston, VA. https://doi.org/10.3133/ds231.
Corazzato, C., Tibaldi, A., 2006. Fracture control on type, morphology and distribution of parasitic volcanic cones: an example from Mt. Etna, Italy. J. Volcanol. Geotherm. Res. 158, 177–194. https://doi.org/10.1016/j.jvolgeores.2006.04.018.
Crown, D.A., Zimbelman, J.R., Williams, D.A., 2021. In: Zimbelman, J.R., Crown, D.A., Mouginis-Mark, P.J., Gregg, T.K.P. (Eds.), 5 - The Circum-Hellas Province. Elsevier, The Volcanoes of Mars, pp. 92–120. https://doi.org/10.1016/B978-0-12-822876-0.00003-5.
Cuřín, V., Brož, P., Hauber, E., Markonis, Y., 2023. Mud flows in Southwestern Utopia Planitia, Mars. Icarus 389. https://doi.org/10.1016/j.icarus.2022.115266.
Dahren, B., Troll, V.R., Andersson, U.B., Chadwick, J.P., Gardner, M.F., Jaxybulatov, K., Koulakov, I., 2012. Magma plumbing beneath Anak Krakatau volcano, Indonesia: evidence for multiple magma storage regions. Contrib. Mineral. Petrol. 163, 631–651. https://doi.org/10.1007/s00410-011-0690-8.
Dapremont, A.M., Wray, J.J., 2021. Igneous or mud volcanism on Mars? The case study of Hephaestus Fossae. J. Geophys. Res. Planets 126. https://doi.org/10.1029/2020JE006390.
De Haas, T., Hauber, E., Kleinhans, M.G., 2013. Local late Amazonian boulder breakdown and denudation rate on Mars. Geophys. Res. Lett. 40, 3527–3531. https://doi.org/10.1002/grl.50726.
De Toffoli, B., Pozzobon, R., Mazzarini, F., Orgel, C., Massironi, M., Giacomini, L., Mangold, N., Cremonese, G., 2018. Estimate of depths of source fluids related to mound fields on Mars. Planet. Space Sci. 164, 164–173. https://doi.org/10.1016/j.pss.2018.07.005.
Ding, N., Bray, V.J., McEwen, A.S., Mattson, S.S., Okubo, C.H., Chojnacki, M., Tornabene, L.L., 2015. The central uplift of Ritchey crater, Mars. Icarus 252, 255–270. https://doi.org/10.1016/j.icarus.2014.11.001.
Dohm, J.M., Tanaka, K.L., 1999. Geology of the Thaumasia region, Mars: plateau development, valley origins, and magmatic evolution. Planet. Space Sci. 47, 411–431. https://doi.org/10.1016/s0032-0633(98)00141-x.
Dohm, J.M., Tanaka, K.L., Hare, T.M., 2001. Geologic, paleotectonic, and paleoerosional maps of the Thaumasia region, Mars, scale 1:5,000,000. U.S. Geol. Surv. Geol. Invest. Ser.
Dohm, J.M., Anderson, R.C., Williams, J.P., Ruiz, J., McGuire, P.C., Buczkowski, D.L., Wang, R., Scharenbroich, L., Hare, T.M., Connerney, J.E.P., Baker, V.R., Wheelock, S.J., Ferris, J.C., Miyamoto, H., 2009. Claritas rise, Mars: pre-Tharsis magmatism? J. Volcanol. Geotherm. Res. 185, 139–156. https://doi.org/10.1016/j.jvolgeores.2009.03.012.
Edgett, K.S., 1990. Possible cinder cones near the summit of Pavonis Mons, Mars. In: Lunar and Planetary Science Conference, pp. 311–312.
Ehlmann, B.L., Mustard, J.F., Swayze, G.A., Clark, R.N., Bishop, J.L., Poulet, F., Des Marais, D.J., Roach, L.H., Milliken, R.E., Wray, J.J., Barnouin-Jha, O., Murchie, S.L., 2009. Identification of hydrated silicate minerals on Mars using MRO-CRISM: geologic context near Nili Fossae and implications for aqueous alteration. J. Geophys. Res. Planets 114, 1–33. https://doi.org/10.1029/2009JE003339.
Fergason, R.L., Hare, T.M., Laura, J., 2018. HRSC and MOLA Blended Digital Elevation Model at 200m v2. [WWW Document]. Astrogeology PDS Annex. U.S. Geol. Surv. URL http://bit.ly/HRSC_MOLA_Blend_v0.
Fink, J., Anderson, S.W., 1999. Lava domes and coulees. In: Sigurdsson, H., Houghton, B., Rymer, H., Stix, J., McNutt, S. (Eds.), Encyclopedia of Volcanoes. Elsevier, pp. 307–320.
Flahaut, J., Mustard, J.F., Quantin, C., Clenet, H., Allemand, P., Thomas, P., 2011. Dikes of distinct composition intruded into Noachian - aged crust exposed in the walls of Valles Marineris. Geophys. Res. Lett. 38, 1–7. https://doi.org/10.1029/2011GL048109.
Fritz, J., Artemieva, N., Greshake, A., 2005. Ejection of Martian meteorites. Meteorit. Planet. Sci. 40, 1393–1411. https://doi.org/10.1111/j.1945-5100.2005.tb00409.x.
Gonnermann, H.M., Manga, M., 2003. Explosive volcanism may not be an inevitable consequence of magma fragmentation. Nature 426, 432–435. https://doi.org/10.1038/nature02138.
Grosse, P., van Wyk de Vries, B., Euillades, P.A., Kervyn, M., Petrinovic, I.A., 2012. Systematic morphometric characterization of volcanic edifices using digital elevation models. Geomorphology 136, 114–131. https://doi.org/10.1016/j.geomorph.2011.06.001.
Grott, M., Hauber, E., Werner, S.C., Kronberg, P., Neukum, G., 2005. High heat flux on ancient Mars: evidence from rift flank uplift at Coracis Fossae. Geophys. Res. Lett. 32, 1–4. https://doi.org/10.1029/2005GL023894.
Grott, M., Hauber, E., Werner, S.C., Kronberg, P., Neukum, G., 2007. Mechanical modeling of thrust faults in the Thaumasia region, Mars, and implications for the Noachian heat flux. Icarus 186, 517–526. https://doi.org/10.1016/j.icarus.2006.10.001.
Grott, M., Baratoux, D., Hauber, E., Sautter, V., Mustard, J., Gasnault, O., Ruff, S.W., Karato, S.I., Debaille, V., Knapmeyer, M., Sohl, F., Van Hoolst, T., Breuer, D., Morschhauser, A., Toplis, M.J., 2013. Long-term evolution of the martian crust-mantle system. Space Sci. Rev. 174, 49–111. https://doi.org/10.1007/s11214-012-9948-3.
Gudmundsson, A., Gronvold, K., Óskarsson, N., Larsen, G., Einarsson, P., Brandsdóttir, B., Sigurdsson, O., Saemundsson, K., Tryggvason, E., Thordarson, T., 1992. The 1991 eruption of Hekla, Iceland. Bull. Volcanol. 54, 238–246.
Gwinner, K., Jaumann, R., Hauber, E., Hoffmann, H., Heipke, C., Oberst, J., Neukum, G., Ansan, V., Bostelmann, J., Dumke, A., Elgner, S., Erkeling, G., Fueten, F., Hiesinger, H., Hoekzema, N.M., Kersten, E., Loizeau, D., Matz, K.D., McGuire, P.C., Mertens, V., Michael, G., Pasewaldt, A., Pinet, P., Preusker, F., Reiss, D., Roatsch, T., Schmidt, R., Scholten, F., Spiegel, M., Stesky, R., Tirsch, D., Van Gasselt, S., Walter, S., Wählisch, M., Willner, K., 2016. The High Resolution Stereo Camera (HRSC) of Mars Express and its approach to science analysis and mapping for Mars and its satellites. Planet. Space Sci. 126, 93–138. https://doi.org/10.1016/j.pss.2016.02.014.
Hartmann, W.K., Malin, M., McEwen, A., Carr, M., Soderblom, L., Thomas, P., Danielson, E., James, P., Veverka, J., 1999. Evidence for recent volcanism on mars from crater counts. Nature 397, 586–589. https://doi.org/10.1038/17545.
Hauber, E., Kronberg, P., 2005. The large Thaumasia graben on Mars: is it a rift? J. Geophys. Res. Planets 110, 1–13. https://doi.org/10.1029/2005JE002407.
Hauber, E., Bleacher, J., Gwinner, K., Williams, D., Greeley, R., 2009. The topography and morphology of low shields and associated landforms of plains volcanism in the Tharsis region of Mars. J. Volcanol. Geotherm. Res. 185, 69–95. https://doi.org/10.1016/j.jvolgeores.2009.04.015.
Hauber, E., Brož, P., Jagert, F., Jodowski, P., Platz, T., 2011. Very recent and wide-spread basaltic volcanism on Mars. Geophys. Res. Lett. 38, 1–5. https://doi.org/10.1029/2011GL047310.
Hjartardóttir, A.R., Einarsson, P., Magnúsdóttir, S., Björnsdóttir, T., Brandsdóttir, B., 2016. Fracture systems of the northern volcanic rift zone, Iceland: an onshore part of the mid-Atlantic plate boundary. Geol. Soc. Spec. Publ. 420, 297–314. https://doi.org/10.1144/SP420.1.
Höskuldsson, Á., Óskarsson, N., Pedersen, R., Grönvold, K., Vogfjöro, K., Ólafsdóttir, R., 2007. The millennium eruption of Hekla in February 2000. Bull. Volcanol. 70, 169–182. https://doi.org/10.1007/s00445-007-0128-3.
Hunt, J.A., Mather, T.A., Pyle, D.M., 2020. Morphological comparison of distributed volcanic fields in the Main Ethiopian rift using high-resolution digital elevation models. J. Volcanol. Geotherm. Res. 393, 106732 https://doi.org/10.1016/j.jvolgeores.2019.106732.
Inc, G., 2021. Google Earth Pro (Version 7.3.4.8642, software) [WWW Document]. URL http://www.google.com/earth.
Karátson, D., Favalli, M., Tarquini, S., Fornaciai, A., Wörner, G., 2010. The regular shape of stratovolcanoes: a DEM-based morphometrical approach. J. Volcanol. Geotherm. Res. 193, 171–181. https://doi.org/10.1016/j.jvolgeores.2010.03.012.
Kerber, L., Head, J.W., Madeleine, J.B., Forget, F., Wilson, L., 2011. The dispersal of pyroclasts from Apollinaris Patera, Mars: implications for the origin of the Medusae Fossae Formation. Icarus 216, 212–220. https://doi.org/10.1016/j.icarus.2011.07.035.
Keszthelyi, L., Jaeger, W., McEwen, A., Tornabene, L., Beyer, R.A., Dundas, C., Milazzo, M., 2008. High resolution imaging science experiment (HiRISE) images of volcanic terrains from the first 6 months of the Mars reconnaissance orbiter primary science phase. J. Geophys. Res. Planets 113, E04005. https://doi.org/10.1029/2007JE002968.
Kleinhans, M.G., Markies, H., De Vet, S.J., In't Veld, A.C., Postema, F.N., 2011. Static and dynamic angles of repose in loose granular materials under reduced gravity. J. Geophys. Res. E Planets 116, 1–13. https://doi.org/10.1029/2011JE003865.
Komatsu, G., Okubo, C.H., Wray, J.J., Ojha, L., Cardinale, M., Murana, A., Orosei, R., Chan, M.A., Ormö, J., Gallagher, R., 2016. Small edifice features in Chryse Planitia, Mars: assessment of a mud volcano hypothesis. Icarus 268, 56–75. https://doi.org/10.1016/j.icarus.2015.12.032.
Korme, T., Chorowicz, J., Collet, B., Bonavia, F., 1997. Volcanic vents rooted on extension fractures and their geodynamic implications in the Ethiopian Rift. J. Volcanol. Geotherm. Res. 79, 205–222. https://doi.org/10.1016/S0377-0273(97)00034-6.
Krishnan, V., Kumar, P.S., 2022. Long-lived and continual volcanic eruptions, tectonic activity, pit chains formation, and boulder avalanches in northern Tharsis region: implications for late Amazonian geodynamics and Seismo-tectonic processes on Mars. J. Geophys. Res. Planets 128. https://doi.org/10.1029/2022JE007511 e2022JE007511.
Lagain, A., Benedix, G.K., Servis, K., Baratoux, D., Doucet, L.S., 2021. The Tharsis mantle source of depleted shergottites revealed by 90 million impact craters. Nat. Commun. 12, 6352. https://doi.org/10.1038/s41467-021-26648-3.
Lapen, T.J., Righter, M., Brandon, A.D., Debaille, V., Beard, B.L., Shafer, J.T., Peslier, A. H., 2010. A younger age for ALH84001 and its geochemical link to shergottite sources in mars. Science (80-.). 328, 347–351. https://doi.org/10.1126/science.1185395.
Le Corvec, N., Menand, T., Lindsay, J., 2013. Interaction of ascending magma with pre-existing crustal fractures in monogenetic. J. Geophys. Res. Solid Earth 118, 968–984. https://doi.org/10.1002/jgrb.50142.
Lesti, C., Giordano, G., Salvini, F., Cas, R., 2008. Volcano tectonic setting of the intraplate Pliocene-Holocene, Newer Volcanic Province (Southeast Australia): role of crustal fracture zones. J. Geophys. Res. 113, B07407. https://doi.org/10.1029/2007JB005110.
Malin, M.C., Bell, J.F., Cantor, B.A., Caplinger, M.A., Calvin, W.M., Clancy, R.T., Edgett, K.S., Edwards, L., Haberle, R.M., James, P.B., Lee, S.W., Ravine, M.A.,

Thomas, P.C., Wolff, M.J., 2007. Context camera investigation on board the Mars Reconnaissance Orbiter. J. Geophys. Res. Planets 112, E05S04. https://doi.org/10.1029/2006JE002808.
Mangold, N., Loizeau, D., Poulet, F., Ansan, V., Baratoux, D., LeMouelic, S., Bardintzeff, J.M., Platevoet, B., Toplis, M., Pinet, P., Masson, P., Bibring, J.P., Gondet, B., Langevin, Y., Neukum, G., 2010. Mineralogy of recent volcanic plains in the Tharsis region, Mars, and implications for platy-ridged flow composition. Earth Planet. Sci. Lett. 294, 440–450. https://doi.org/10.1016/j.epsl.2009.07.036.
Martí, J., 2019. Las Cañadas caldera, Tenerife, Canary Islands: a review, or the end of a long volcanological controversy. Earth-Sci. Rev. 196 https://doi.org/10.1016/j.earscirev.2019.102889.
McEwen, A.S., Eliason, E.M., Bergstrom, J.W., Bridges, N.T., Hansen, C.J., Delamere, W. A., Grant, J.A., Gulick, V.C., Herkenhoff, K.E., Keszthelyi, L., Kirk, R.L., Mellon, M.T., Squyres, S.W., Thomas, N., Weitz, C.M., Reconnaissance, Mars, 2007. Orbiter's high resolution imaging science experiment (HiRISE). J. Geophys. Res. 112, E05S02. https://doi.org/10.1029/2005JE002605.
McGuire, P.C., Bishop, J.L., Brown, A.J., Fraeman, A.A., Marzo, G.A., Frank Morgan, M., Murchie, S.L., Mustard, J.F., Parente, M., Pelkey, S.M., Roush, T.L., Seelos, F.P., Smith, M.D., Wendt, L., Wolff, M.J., 2009. An improvement to the volcano-scan algorithm for atmospheric correction of CRISM and OMEGA spectral data. Planet. Space Sci. 57, 809–815. https://doi.org/10.1016/j.pss.2009.03.007.
McSween Jr., H.Y., 2015. Petrology on Mars. Am. Mineral. 100, 2380–2395. https://doi.org/10.2138/am-2015-5257.
Melnick, D., Folguera, A., Ramos, V.A., 2006. Structural control on arc volcanism: the Caviahue-Copahue complex, Central to Patagonian Andes transition (38°S). J. S. Am. Earth Sci. 22, 66–88. https://doi.org/10.1016/j.jsames.2006.08.008.
Meresse, S., Costard, F., Mangold, N., Masson, P., Neukum, G., 2008. Formation and evolution of the chaotic terrains by subsidence and magmatism: Hydraotes Chaos, Mars. Icarus 194, 487–500. https://doi.org/10.1016/j.icarus.2007.10.023.
Mittlefehldt, D.W., 1994. ALH84001, a cumulate orthopyroxenite member of the martian meteorite clan. Meteoritics 221, 214–221. https://doi.org/10.1111/j.1945-5100.1994.tb00673.x.
Morgan, M.F., Seelos, F.P., Murchie, S.L., 2017. The CRISM Analysis Toolkit (CAT): Overview and Recent Updates. In: in: LPI Editorial Board (Ed.), Third Planetary Data Workshop and The Planetary Geologic Mappers Annual Meeting, LPI Contributions.
Mouginis-Mark, P.J., Crown, D.A., Zimbelman, J.R., Williams, D.A., 2021. In: Zimbelman, J.R., Crown, D.A., Mouginis-Mark, P.J., Gregg, T.K.P. (Eds.), 3 - The Tharsis Province. Elsevier, The Volcanoes of Mars, pp. 36–68. https://doi.org/10.1016/B978-0-12-822876-0.00013-8.
Murchie, S., Arvidson, R., Bedini, P., Beisser, K., Bibring, J.P., Bishop, J., Boldt, J., Cavender, P., Choo, T., Clancy, R.T., Darlington, E.H., Des Marais, D., Espiritu, R., Fort, D., Green, R., Guinness, E., Hayes, J., Hash, C., Heffernan, K., Hemmler, J., Heyler, G., Humm, D., Hutcheson, J., Izenberg, N., Lee, R., Lees, J., Lohr, D., Malaret, E., Martin, T., McGovern, J.A., McGuire, P., Morris, R., Mustard, J., Pelkey, S., Rhodes, E., Robinson, M., Roush, T., Schaefer, E., Seagrave, G., Seelos, F., Silverglate, P., Slavney, S., Smith, M., Shyong, W.J., Strohbehn, K., Taylor, H., Thompson, P., Tossman, B., Wirzburger, M., Wolff, M., 2007. Compact connaissance imaging spectrometer for Mars (CRISM) on Mars Reconnaissance Orbiter (MRO). J. Geophys. Res. E Planets 112, 1–57. https://doi.org/10.1029/2006JE002682.
Murchie, S.L., Seelos, F.P., Hash, C.D., Humm, D.C., Malaret, E., McGovern, J.A., Choo, T.H., Seelos, K.D., Buczkowski, D.L., Morgan, M.F., Barnouin-Jha, O.S., Nair, H., Taylor, H.W., Patterson, G.W., Harvel, C.A., Mustard, J.F., Arvidson, R.E., McGuire, P., Smith, M.D., Wolff, M.J., Titus, T.N., Bibring, J.P., Poulet, F., 2009. Compact Reconnaissance imaging spectrometer for Mars investigation and data set from the Mars Reconnaissance Orbiter's primary science phase. J. Geophys. Res. Planets 114, 1–15. https://doi.org/10.1029/2009JE003344.
Mustard, J.F., Poulet, F., Gendrin, A., Bibring, J., Langevin, Y., Gondet, B., Mangold, N., 2005. Olivine and pyroxene diversity in the crust of Mars. Scien 307, 1594–1598.
Neukum, G., Jaumann, R., Hoffmann, H., Hauber, E., Head, J.W., Basilevsky, A.T., Ivanov, B.A., Werner, S.C., Van Gasselt, S., 2004. Recent and episodic volcanic and glacial activity on Mars revealed by the High Resolution Stereo Camera. Nature 432, 971–979. https://doi.org/10.1038/nature03231.
Okubo, C.H., 2016. Morphologic evidence of subsurface sediment mobilization and mud volcanism in Candor and Coprates Chasmata, Valles Marineris, Mars. Icarus 269, 23–37. https://doi.org/10.1016/j.icarus.2015.12.051.
Opheim, J.A., Gudmundsson, A., 1989. Formation and geometry of fractures, and related volcanism, of the Krafla fissure swarm, Northeast Iceland. Geol. Soc. Am. Bull. 101, 1608–1622. https://doi.org/10.1130/0016-7606(1989)101<1608:FAGOFA>2.3.CO;2.
Papike, J.J., Karner, J.M., Shearer, C.K., Burger, P.V., 2009. Silicate mineralogy of martian meteorites. Geochim. Cosmochim. Acta 73, 7443–7485. https://doi.org/10.1016/j.gca.2009.09.008.
Parente, M., Makarewicz, H.D., Bishop, J.L., 2011. Decomposition of mineral absorption bands using nonlinear least squares curve fitting: application to Martian meteorites and CRISM data. Planet. Space Sci. 59, 423–442. https://doi.org/10.1016/j.pss.2011.01.009.
Paulsen, T.S., Wilson, T.J., 2010. New criteria for systematic mapping and reliability assessment of monogenetic volcanic vent alignments and elongate volcanic vents for crustal stress analyses. Tectonophysics 482, 16–28. https://doi.org/10.1016/j.tecto.2009.08.025.
Pedersen, G.B.M., Grosse, P., Gudmundsson, M.T., 2020. Morphometry of glaciovolcanic edifices from Iceland: types and evolution. Geomorphology 370, 107334. https://doi.org/10.1016/j.geomorph.2020.107334.
Pelkey, S.M., Mustard, J.F., Murchie, S., Clancy, R.T., Wolff, M., Smith, M., Milliken, R. E., Bibring, J.P., Gendrin, A., Poulet, F., Langevin, Y., Gondet, B., 2007. CRISM multispectral summary products: parameterizing mineral diversity on Mars from reflectance. J. Geophys. Res. Planets 112. https://doi.org/10.1029/2006JE002831.
Peters, S.I., Christensen, P.R., Clarke, A.B., 2021. Lava flow eruption conditions in the Tharsis Volcanic Province on Mars. J. Geophys. Res. Planets 126. https://doi.org/10.1029/2020JE006791.
Pieterek, B., Ciazela, J., Lagain, A., Ciazela, M., 2022a. Late Amazonian dike-fed distributed volcanism in the Tharsis volcanic province on Mars. Icarus 386, 115151. https://doi.org/10.1016/j.icarus.2022.115151.
Pieterek, B., Laban, M., Ciążela, J., Muszyński, A., 2022b. Explosive volcanism in Noctis fossae on Mars. Icarus 375, 114851. https://doi.org/10.1016/j.icarus.2021.114851.
Platz, T., Münn, S., Walter, T.R., Procter, J.N., McGuire, P.C., Dumke, A., Neukum, G., 2011. Vertical and lateral collapse of Tharsis Tholus. Mars. Earth Planet. Sci. Lett. 305, 445–455. https://doi.org/10.1016/j.epsl.2011.03.012.
Plesa, A.C., Padovan, S., Tosi, N., Breuer, D., Grott, M., Wieczorek, M.A., Spohn, T., Smrekar, S.E., Banerdt, W.B., 2018. The thermal state and interior structure of Mars. Geophys. Res. Lett. 45, 12,198–12,209. https://doi.org/10.1029/2018GL080728.
Plesa, A.C., Wieczorek, M., Knapmeyer, M., Rivoldini, A., Bozdag, E., Walterova, M., Knapmeyer-Endrun, B., Kim, D., Broquet, A., Stähler, S., Mittelholtz, A., Breuer, D., Johnson, C.L., Hauber, E., Panning, M., Spohn, T., Lognonné, P., Smrekar, S.E., Banerdt, W.B., 2023. InSight Science Team, 2023. Insight's constraints on the interior of Mars: geodynamical models and observations. In: 54th Lunar Planetary Science Conference, p. 2212.
Plescia, J.B., 2004. Morphometric properties of Martian volcanoes. J. Geophys. Res. Planets 109, E03003. https://doi.org/10.1029/2002je002031.
Plescia, J.B., Saunders, R.S., 1982. Tectonic history of the Tharsis Region, Mars. J. Geophys. Res. 87, 9775. https://doi.org/10.1029/jb087ib12p09775.
Poulet, F., Mangold, N., Platevoet, B., Bardintzeff, J.M., Sautter, V., Mustard, J.F., Bibring, J.P., Pinet, P., Langevin, Y., Gondet, B., Aléon-Toppani, A., 2009. Quantitative compositional analysis of martian mafic regions using the MEx/OMEGA reflectance data. 2. Petrological implications. Icarus 201, 84–101. https://doi.org/10.1016/j.icarus.2008.12.042.
Quantin, C., Flahaut, J., Clenet, H., Allemand, P., Thomas, P., 2012. Composition and structures of the subsurface in the vicinity of Valles Marineris as revealed by central uplifts of impact craters. Icarus 221, 436–452. https://doi.org/10.1016/j.icarus.2012.07.031.
Quantin-Nataf, C., Lozac, L., Thollot, P., Loizeau, D., Bultel, B., Fernando, J., Allemand, P., Dubuffet, F., Poulet, F., Ody, A., Clenet, H., Leyrat, C., Harrisson, S., 2018. MarsSI: Martian surface data processing information system. Planet. Space Sci. 150, 157–170. https://doi.org/10.1016/j.pss.2017.09.014.
Reynolds, P., Brown, R.J., Thordarson, T., Llewellin, E.W., 2016. The architecture and shallow conduits of Laki-type pyroclastic cones: insights into a basaltic fissure eruption. Bull. Volcanol. 78 https://doi.org/10.1007/s00445-016-1029-0.
Richardson, J.A., Bleacher, J.E., Glaze, L.S., 2013. The volcanic history of Syria Planum, Mars. J. Volcanol. Geotherm. Res. 252, 1–13. https://doi.org/10.1016/j.jvolgeores.2012.11.007.
Richardson, J.A., Bleacher, J.E., Connor, C.B., Glaze, L.S., 2021. Small volcanic vents of the Tharsis Volcanic Province, Mars. J. Geophys. Res. Planets 126. https://doi.org/10.1029/2020JE006620 e2020JE006620.
Robbins, S.J., Di Achille, G., Hynek, B.M., 2011. The volcanic history of Mars: high-resolution crater-based studies of the calderas of 20 volcanoes. Icarus 211, 1179–1203. https://doi.org/10.1016/j.icarus.2010.11.012.
Rossi, A.P., van Gasselt, S., Pondrelli, M., Dohm, J., Hauber, E., Dumke, A., Zegers, T., Neukum, G., 2011. Evolution of periglacial landforms in the ancient mountain range of the Thaumasia Highlands. Mars. Geol. Soc. Spec. Publ. 356, 69–85. https://doi.org/10.1144/SP356.5.
Ruff, S.W., Christensen, P.R., 2002. Bright and dark regions on Mars: particle size and mineralogical characteristics based on thermal emission spectrometer data. J. Geophys. Res. Planets 107, 1–22. https://doi.org/10.1029/2001je001580.
Ruj, T., Kawai, K., 2021. A global investigation of wrinkle ridge formation events; implications towards the thermal evolution of Mars. Icarus 369, 114625. https://doi.org/10.1016/j.icarus.2021.114625.
Schultz, R.A., Tanaka, K.L., 1994. Lithospheric-scale buckling and thrust structures on Mars: the Coprates rise and south Tharsis ridge belt. J. Geophys. Res. 99, 8371–8385. https://doi.org/10.1029/94JE00277.
Shevchenko, A.V., Dvigalo, V.N., Walter, T.R., Mania, R., Maccaferri, F., Svirid, I.Y., Belousov, A.B., Belousova, M.G., 2020. The rebirth and evolution of Bezymianny volcano, Kamchatka after the 1956 sector collapse. Commun. Earth Environ. 1, 1–15. https://doi.org/10.1038/s43247-020-00014-5.
Skok, J.R., Mustard, J.F., Tornabene, L.L., Pan, C., Rogers, D., Murchie, S.L., 2012. A spectroscopic analysis of Martian crater central peaks: formation of the ancient crust. J. Geophys. Res. E Planets 117. https://doi.org/10.1029/2012JE004148.
Smith, D.E., Zuber, M.T., Frey, H.V., Garvin, J.B., Head, J.W., Muhleman, D.O., Pettengill, G.H., Phillips, R.J., Solomon, S.C., Zwally, H.J., Banerdt, W.B., Duxbury, T.C., Golombek, M.P., Lemoine, F.G., Neumann, G.A., Rowlands, D.D., Aharonson, O., Ford, P.G., Ivanov, A.B., Johnson, C.L., McGovern, P.J., Abshire, J.B., Afzal, R.S., Sun, X., 2001. Mars orbiter laser altimeter: experiment summary after the first year of global mapping of Mars. J. Geophys. Res. Planets 106, 23,689–23,722. https://doi.org/10.1029/2000JE001364.
Smith, M.R., Gillespie, A.R., Montgomery, D.R., Batbaatar, J., 2009. Crater-fault interactions: a metric for dating fault zones on planetary surfaces. Earth Planet. Sci. Lett. 284, 151–156. https://doi.org/10.1016/j.epsl.2009.04.025.
Tadini, A., Bevilacqua, A., Neri, A., Cioni, R., Aspinall, W.P., Bissom, M., Isaia, R., Mazzarini, F., Valentine, G.A., Vitale, S., Baxter, P.J., Bertagnini, A., Cerminara, M., de Michieli Vitturi, M., Di Roberto, A., Engwell, S., Esposti Ongaro, T., Flandoli, F., Pistolesi, M., 2017. Assessing future vent opening locations at the Somma-Vesuvio volcanic complex: 2. Probability maps of the caldera for a future Plinian/sub-Plinian

event with uncertainty quantification. J. Geophys. Res. Solid Earth 122, 4357–4376. https://doi.org/10.1002/2016JB013860.
Tanaka, K.L., Davis, P.A., 1988. Tectonic history of the Syria Planum province of Mars. J. Geophys. Res. 93, 893–917. https://doi.org/10.1029/jb093ib12p14893.
Tanaka, K.L., Robbins, S.J., Fortezzo, C.M., Skinner, J.A., Hare, T.M., 2014. The digital global geologic map of Mars: chronostratigraphic ages, topographic and crater morphologic characteristics, and updated resurfacing history. Planet. Space Sci. 95, 11–24. https://doi.org/10.1016/j.pss.2013.03.006.
Tibaldi, A., Bonali, F.L., Corazzato, C., 2017. Structural control on volcanoes and magma paths from local- to orogen-scale: the Central Andes case. Tectonophysics 699, 16–41. https://doi.org/10.1016/j.tecto.2017.01.005.
Vaz, D.A., Spagnuolo, M.G., Silvestro, S., 2014. Morphometric and geometric characterization of normal faults on Mars. Earth Planet. Sci. Lett. 401, 83–94. https://doi.org/10.1016/j.epsl.2014.05.022.
Viviano, C.E., Murchie, S.L., Daubar, I.J., Morgan, M.F., Seelos, F.P., Plescia, J.B., 2019. Composition of Amazonian volcanic materials in Tharsis and Elysium, Mars, from MRO/CRISM reflectance spectra. Icarus 328, 274–286. https://doi.org/10.1016/j.icarus.2019.03.001.
Viviano-Beck, C.E., Seelos, F.P., Murchie, S.L., Kahn, E.G., Seelos, K.D., Taylor, H.W., Taylor, K., Ehlmann, B.L., Wisemann, S.M., Mustard, J.F., Morgan, M.F., 2014. Revised CRISM spectral parameters and summary products based on the currently detected mineral diversity on Mars. J. Geophys. Res. Planets 119, 1403–1431. https://doi.org/10.1002/2014JE004627.
Viviano-Beck, C.E., Murchie, S.L., Beck, A.W., Dohm, J.M., 2017. Compositional and structural constraints on the geologic history of eastern Tharsis rise, Mars. Icarus 284, 43–58. https://doi.org/10.1016/j.icarus.2016.09.005.
Werner, S.C., 2009. The global martian volcanic evolutionary history. Icarus 201, 44–68. https://doi.org/10.1016/j.icarus.2008.12.019.
Wilson, L., 2009. Volcanism in the solar system. Nat. Geosci. 2, 389–397. https://doi.org/10.1038/ngeo529.
Wilson, L., Head, J.W., 1994. Mars: review and analysis of volcanic eruption theory and relationships to observed landforms. Rev. Geophys. 32, 221–263. https://doi.org/10.1029/94RG01113.
Wilson, L., Head, J.W., 2007. Explosive volcanic eruptions on Mars: tephra and accretionary lapilli formation, dispersal and recognition in the geologic record. J. Volcanol. Geotherm. Res. 163, 83–97. https://doi.org/10.1016/j.jvolgeores.2007.03.007.
Wilson, L., Scott, E.D., Head III, J.W., 2001. Evidence for episodicity in the magma supply to the large Tharsis volcanoes. J. Geophys. Res. 106, 1423–1433. https://doi.org/10.1029/2000JE001280.
Xiao, L., Huang, J., Christensen, P.R., Greeley, R., Williams, D.A., Zhao, J., He, Q., 2012. Ancient volcanism and its implication for thermal evolution of Mars. Earth Planet. Sci. Lett. 323–324, 9–18. https://doi.org/10.1016/j.epsl.2012.01.027.
Zimbelman, J.R., Garry, W.B., Bleacher, J.E., Crown, D.A., 2015. Volcanism on Mars. In: Sigurdsson, I.A., Houghton, B., McNutt, S.R., Rymer, H., Stix, J. (Eds.), The Encyclopedia of Volcanoes. Elsevier, pp. 717–729.